

Earth ArXiv



1 This is a non-peer-reviewed preprint submitted to EarthArXiv.

2

3

4

5

6

7 This manuscript has been submitted for publication in
8 *Communications Earth & Environment*. Please note the manuscript
9 has yet to be formally accepted for publication. Subsequent
10 versions of this manuscript may have slightly different content. If
11 accepted, the final version of this manuscript will be available via
12 the 'Peer-reviewed Publication DOI' link on the right-hand side of
13 this webpage. Please feel free to contact any of the authors; we
14 welcome feedback.

15

16

17

18

19 Calcium promotes carbon rich grassland soils

20 Slessarev, E.W.,^{1,2*} Goertzen, H.R.,³ Lybrand, R.,³ McFarlane, K.J.,⁴ Pett-Ridge, J.^{4,5,6}, Sokol,
 21 N.⁴, Zaharescu, D.³ Georgiou, K.,⁷

22

¹ Department of Ecology and Evolutionary Biology, Yale University, New Haven, CT, USA

²⁴ ² Yale Center for Natural Carbon Capture, Yale University, New Haven, CT, USA ³ Department
²⁵ of Biological and Ecological Engineering, Oregon State University, Corvallis, OR, USA

26 ³ Department of Land Air and Water Resources, University of California, Davis, CA, USA

²⁷ ⁴ Physical and Life Sciences Directorate, Lawrence Livermore National Laboratory, Livermore,
²⁸ CA, USA

²⁹ ⁵ Innovative Genomics Institute, University of California Berkeley, Berkeley, CA.

⁶ Life & Environmental Sciences Department, University of California Merced, Merced, CA 95344, USA

⁷ Department of Biological and Ecological Engineering, Oregon State University, Corvallis, OR

32 USA
33

33

34

35

35

36 **Abstract**

37 **Dark colored grassland soils, known as Mollisols, are intensively farmed and exceptionally**
38 **rich in organic matter, and hence have an important role in the carbon cycle. Elevated carbon**
39 **storage in Mollisols may be facilitated by calcium (Ca) released by carbonate and silicate**
40 **weathering. This synergy between carbon and calcium cycling has yet to be tested at scale.**
41 **To close this knowledge gap, we developed a novel geochemical model and leveraged**
42 **continental-scale datasets to simulate Ca release in soils across the USA. We found that Ca**
43 **released by mineral weathering helps to predict the distribution of Mollisols and soil organic**
44 **carbon storage. Our model also indicates that agriculture has increased Ca inputs to**
45 **cultivated USA Mollisols 2-5 fold, demonstrating that humans have fundamentally changed**
46 **the geochemical conditions that sustain carbon storage in these soils. By implication,**
47 **moderating the quantity of and timing of Ca release may be essential for sustaining soil**
48 **carbon storage in the world's most intensively farmed landscapes.**

49 **Main**

50 Temperate grasslands feature exceptionally fertile, dark-colored soils known as Mollisols.
51 Mollisols are the world's most intensively farmed soil type.¹ Based on recent data,^{2,3} we estimate
52 that Mollisols comprise only 7% of the Earth's land area yet support 24% of agricultural land and
53 32% of all calories from production of corn, soy, and wheat. Mollisols also contribute
54 disproportionately to soil organic carbon storage, storing 32% of the organic carbon held in Earth's
55 agricultural soils (see Methods). This makes Mollisols critical to land-based climate mitigation
56 efforts. At the same time, Mollisols are disproportionately exposed to environmental threats,
57 including soil erosion,⁴ and have lost a significant fraction of their carbon to cultivation.⁵ Effective
58 stewardship of Mollisols in the face of these threats requires a comprehensive understanding of
59 the environmental factors that make them fertile and carbon rich.

60 There are several ecological processes that contribute to the carbon richness of Mollisols,
61 and these have implications for protecting and restoring soil organic carbon. As early as the 1860's,
62 grassland vegetation was identified as the main driver of Mollisol formation.⁶ Perennial grasses
63 grow extensive fibrous root systems, and root turnover is an important pathway of soil organic
64 carbon accrual.^{7,8} Grasslands and savannas are characterized by frequent fires, and fires can
65 generate persistent pyrogenic carbon that might explain the origin of Mollisols.⁹ Grasslands also
66 support robust populations of burrowing animals that contribute to the thick, carbon-rich topsoil
67 layers characteristic of Mollisols.¹⁰ Contemporary proposals for restoring carbon storage in
68 cropland soils mimic ecological processes that are thought to be important in Mollisols; for
69 instance, carbon sequestration might be achieved by returning deep rooted cultivars to croplands,¹¹
70 increasing plant diversity,¹² or amending soils with pyrogenic carbon.¹³

71 Geologic factors can also help to explain the origins of Mollisols. Mollisols are commonly
72 formed from calcareous rocks or from aeolian deposits rich in calcium carbonate.⁶ A growing body
73 of evidence shows that Ca stabilizes soil organic matter. Ca facilitates sorption of organic
74 molecules on clays and promotes the growth of bacterial biofilms that are retained on mineral
75 surfaces.¹⁴⁻¹⁶ These processes manifest at continental scales, where soil organic carbon is spatially
76 correlated with exchangeable Ca²⁺, i.e., Ca²⁺ that is reversibly bound to surfaces as an
77 exchangeable cation.^{17,18} The relative abundance of exchangeable Ca²⁺ and other base cations
78 (Mg²⁺, K⁺, and Na⁺) is important in classifying Mollisols, reflecting their role in Mollisol genesis.¹⁹
79 These facts suggest that judicious management of soil Ca availability might also be a tool to
80 promote organic carbon storage, although this possibility has received relatively scant attention.
81 This is in part because the availability of Ca²⁺ in soil is a function of complex interactions among

82 vegetation, geology, and climate. This makes it challenging to disentangle the role of Ca from other
83 drivers of carbon storage in Mollisols.

84 We addressed the role of Ca in Mollisol organic carbon storage by developing and applying
85 a novel geochemical model across the conterminous USA. Our modeling approach leveraged soil
86 mineralogy data available across the USA,²⁰ which enabled us to represent soil chemical processes
87 at an unprecedented spatial extent. We designed our model to track the inputs and outputs of major
88 cations and anions to the soil solution, allowing us to simulate soil pH, mineral weathering rates,
89 and associated Ca release and retention. We used the model to quantify specific Ca sources:
90 carbonate weathering, silicate weathering, and atmospheric deposition. We then statistically
91 estimated the effect of each source on Mollisol extent and carbon storage while accounting for
92 vegetation and climate. Using this approach, we isolated the effect of specific geologic Ca sources
93 on Mollisols and quantified the role of Ca in sustaining Mollisol organic carbon stocks.

94 **Geochemical model performance**

95 We used our geochemical model to estimate the input of available Ca to soil across the
96 conterminous USA and then related Ca inputs to: (1) Mollisol extent, derived from ground based
97 soil classification and mapping²¹ (Figure 1a); and (2) observations of topsoil (A-horizon) organic
98 carbon stocks^{22,23} (Figure 1b). We first parametrized the model with input data including climate,
99 atmospheric deposition of major solutes, net primary productivity, agricultural element budgets,
100 and soil mineralogy (see Methods). The model integrated these variables by linking inputs and
101 outputs of solutes, the release of CO₂ and organic acids by biota, and mineral weathering via a set
102 of pH-dependent equilibrium reactions. We calibrated two unconstrained parameters related to
103 mineral surface reactivity, training the model to match modern observations of soil pH. The model
104 performed relatively well, explaining 69% of the spatial variation in depth-averaged soil pH (0-

105 100 cm), 39% of the variation in soil exchangeable Ca^{2+} , and 64% of the variation across all
106 exchangeable ions when applied to a separate validation set of ground observations (Figure S1,
107 Figure S2, Table S1). We re-parametrized the model to reflect preindustrial (1850) rates of
108 atmospheric deposition²⁴ and eliminated agricultural processes following calibration and
109 validation steps. We then simulated Ca release from carbonate and silicate weathering and
110 exchangeable Ca^{2+} under pre-industrial conditions.

111 **Environmental controls on Mollisols**

112 Our geochemical model shows that Mollisol extent correlates with the inputs of available Ca
113 (Figure 1c) and also with the presence of grassland vegetation (Figure 1d). To disentangle these
114 correlations, we applied a multivariate logistic regression, quantifying the present-day influence
115 of Ca on the geographic distribution of Mollisols while accounting for vegetation and other climate
116 and soil factors. We used the base saturation percentage to represent the influence of Ca in the
117 regression because this index is one of several factors used to classify and map Mollisols in the
118 USA¹⁹ [base saturation = 100*(total base cation charge / cation exchange capacity)]. We also
119 included six additional factors: (1) the pre-agricultural grassland and savanna distribution, which
120 we approximated with a potential vegetation map derived from remotely sensed patches of relict
121 vegetation;²⁵ (2) mean annual temperature; (3) mean annual precipitation; (4) soil silt and clay
122 content (5) soil drainage class; (6) net primary productivity. We compared the independent
123 explanatory power of these factors by computing scaled regression coefficients (Table S2). The
124 regression model matched the observations relatively well, classifying 79% of locations correctly.
125 We found that base saturation was the strongest predictor of the distribution of Mollisols, followed
126 by grassland and savanna presence, mean annual air temperature, precipitation, and other soil

127 properties (Figure 2a). Together, these results indicate that Mollisols are associated with grassland
128 environments rich in Ca^{2+} and other base cations, particularly in drier and cooler climates.

129 Our results indicate that base cations, including Ca^{2+} , are an important control on the
130 distribution of Mollisols. However, these results are not direct evidence that Ca enhances Mollisol
131 organic carbon storage; rather, they show that the relative abundance of exchangeable Ca^{2+} and
132 other base cations strongly influences where Mollisols are mapped. To address the role of Ca in
133 organic carbon storage directly, we related modeled exchangeable Ca^{2+} to soil carbon stock data
134 retrieved from two databases, the US Department of Agriculture Rapid Carbon Assessment and
135 the National Cooperative Soil Survey archives.^{22,23} We used these data to quantify A-horizon
136 organic carbon stocks across the USA (Figure 1b). Mollisols are characterized by thick, carbon-
137 rich A-horizons;¹⁹ hence we used total A-horizon carbon—incorporating both topsoil thickness
138 and carbon content—to quantify the primary mode of carbon storage in Mollisols.

139 We related A-horizon organic carbon stocks to total exchangeable Ca^{2+} using multiple
140 linear regression. We also included the same set of variables used for interpreting Mollisol extent,
141 plus the sum of non-Ca exchangeable cations (Mg^{2+} , K^+ , Na^+ , Al^{3+} , and H^+). The regression model
142 explained 30% of the variation in A-horizon organic carbon stocks. Comparison of the scaled
143 regression coefficients revealed that net primary productivity and temperature were the most
144 important predictors of A-horizon carbon storage, followed by exchangeable Ca^{2+} , the presence of
145 grasslands or savannas, and then other factors (Figure 2b; Table S3). The controls on A-horizon
146 carbon storage across the conterminous USA are distinct from the controls on Mollisol extent
147 because Mollisols are not the only soil types that feature carbon-rich topsoil. For instance, cool,
148 productive forests in the northwestern USA accumulate soil organic carbon due to high organic
149 matter inputs, inhibition of decomposition by low temperatures, and abundant reactive Al and Fe

150 minerals.²⁶ It is nonetheless clear that exchangeable Ca^{2+} is an important secondary control on A-
151 horizon carbon storage. Furthermore, the combined effect of other exchangeable ions was weak,
152 suggesting that it is specifically Ca, rather than total cation exchange capacity, that contributes to
153 A-horizon carbon storage.

154 Our regression analysis identifies a major role for Ca in Mollisol function, but also suggests
155 that grassland and savanna vegetation influence the distribution of Mollisols independent of other
156 factors. Grasslands and savannas can be maintained by fire, helping grasses to persist in climates
157 that would otherwise support forest.^{27,28} In this case, fire regimes that maintain grass dominance
158 might directly determine where Mollisols form. On the other hand, Mollisols are notably
159 uncommon in tropical grasslands and savannas,²⁹ which suggests that ecological factors common
160 to grasslands and savannas—including high belowground productivity and fire—are not sufficient
161 to generate Mollisols. Tropical soils are typically highly weathered, host less reactive minerals,
162 and are generally more acidic than temperate soils that received Ca-rich minerals following
163 Pleistocene glaciation.^{30,31} These geologic limits to Ca supply, in addition to climate, may curtail
164 Mollisol development in the tropics. By contrast, multiple overlapping environmental factors—
165 including Ca weathering in post-glacial soils, cooler temperatures, mesic climate, and the presence
166 of grasses—converge in certain temperate regions, and Mollisols are an emergent result of these
167 overlapping factors.

168 **Identifying ultimate geologic drivers of Mollisol carbon storage**

169 Our geochemical model enabled us to consider the specific geologic mechanisms that explain the
170 distribution of Mollisols. We evaluated the effect of Ca sources on Mollisol extent by constructing
171 counterfactual scenarios in which Ca sources were suppressed under simulated preindustrial
172 conditions. Specifically, we (1) set carbonate weathering, all silicate weathering, or atmospheric

173 Ca deposition to zero in the geochemical model, (2) used updated outputs from the geochemical
174 model to generate predictions using the previously fitted logistic regression, and (3) quantified
175 changes in the predicted area of Mollisols. For reference, we also created a counterfactual scenario
176 in which all vegetation was assumed to be non-grassland. This analysis revealed that both
177 carbonate and silicate weathering help to explain the presence of Mollisols. In the absence of
178 carbonate weathering, predicted preindustrial Mollisol extent was 4% lower (4 Mha), and without
179 silicate weathering Mollisol extent was 27% lower (52 Mha). When both weathering sources were
180 eliminated, the effect was non-additive: Mollisol extent dropped by 90% (174 Mha), which was
181 comparable to the effect of eliminating grassland vegetation (85%, 166 Mha). By contrast,
182 eliminating atmospheric Ca deposition reduced Mollisol extent by only 2% (4 Mha) (Figure 3a).

183 We also evaluated the effects of specific geologic Ca sources on A-horizon organic carbon
184 by eliminating Ca sources in the geochemical model as above. This analysis indicated that
185 carbonate and silicate weathering jointly promote A-horizon soil organic carbon storage. Across
186 the conterminous USA, predicted preindustrial A-horizon carbon storage was 5% (1.2 Pg C) lower
187 when carbonate weathering was eliminated, 2% (0.6 Pg C) lower when silicate weathering was
188 eliminated, and 11% (2.9 Pg C) lower when both were eliminated together (Figure 3b). This
189 combined effect was similar to eliminating grassland vegetation, which reduced A-horizon organic
190 carbon storage by 10% (2.7 Pg C) (Figure 3b). When we focused our analysis on Mollisol regions
191 specifically, we found A-horizon organic carbon stocks were even more sensitive to eliminating
192 carbonate and silicate weathering (16% reduction, 1.2 Pg C) and grassland vegetation (19%, 1.5
193 Pg C).

194 Taken together, our results show that carbonate weathering and silicate weathering have
195 modest effects on Mollisol extent and A-horizon carbon storage when considered alone, but a more

196 substantial effect when combined at a continental scale. This result emerges because carbonate
197 weathering and silicate weathering suppress each other via their alkalizing effect on soil pH; hence
198 eliminating one Ca source yields a compensatory increase in Ca release from the other.
199 Consequently, when either silicates or carbonates are sufficiently abundant, soil Ca^{2+} availability
200 is high and Ca^{2+} generally predominates over other exchangeable ions. These conditions favor
201 Mollisol formation and organic carbon accrual across a range of geologic settings.

202 Our model suggests that the elevated Ca inputs that generate Mollisols in the
203 midcontinental USA are derived from specific geologic sources, particularly carbonate minerals
204 (Figure 3b). Glacial deposition explains elevated carbonate weathering in the north-central USA,
205 where lobes of the Laurentide ice sheet ground up and distributed underlying limestone and
206 dolomite rocks during the last ice age.³² Farther south, soil carbonates are abundant in the aeolian
207 Bignell Loess deposits³³ and in the predominately limestone rocks of the Edwards Plateau,³⁴ both
208 of which support Mollisols. Carbonate minerals are also abundant in the arid Western USA;
209 however, our geochemical model predicts that carbonates are either a minor source or a Ca sink in
210 this region (Figure S3). While some of the carbonates in these soils may be derived from
211 sedimentary rocks, desert carbonates are often primarily derived from in-situ precipitation of
212 CaCO_3 from aeolian Ca.³⁵ Our model suggests that some of these carbonates may be slowly
213 weathering under late-Holocene conditions, supplying Ca to overlying Mollisols.

214 Our model also predicts that inputs of Ca from deposition are significant in much of the
215 USA (Figure 3c); however, we found that atmospheric deposition of Ca is a minor control on
216 Mollisol extent (Figure 3a). We assumed that preindustrial Ca deposition was five-fold lower in
217 North America than at present based on paleo dust records.³⁶ Dust fluxes in the midcontinental
218 USA were substantially higher in the late Pleistocene than in recent preindustrial times due to

219 glaciation.³⁷ Ca in modern soil carbonates is often inherited from Pleistocene dust,³⁸ and
220 carbonates continue to weather in Pleistocene loess deposits. Thus, over geologic timescales,
221 atmospheric Ca deposition during glacial periods may set the stage for future carbonate
222 weathering, helping to build Mollisol organic carbon stocks.

223 **Implications for Mollisol conservation and climate mitigation**

224 Our results imply that changes in soil Ca inputs due to cultivation might affect organic carbon
225 cycling in Mollisols. To address this possibility, we used our model to evaluate the magnitude of
226 changes to the Ca balance of Mollisol croplands relative to preindustrial conditions. We
227 parametrized the model with modern day atmospheric deposition chemistry, enabled agricultural
228 fertilizer addition and nutrient removal, and estimated agricultural liming rates. This analysis
229 shows that soil Ca cycling has changed dramatically in two ways (Figure 4). First, the model
230 predicts that acid inputs from fertilizer and atmospheric deposition have accelerated Ca release
231 from carbonate weathering by 23% (\pm 20%) in Mollisols. Second, agricultural liming has
232 massively increased Ca inputs to cropland soils (Figure 4). Taking modeled liming rates as a
233 reference point, agriculture has more than doubled Ca inputs to Mollisol cropland soils and
234 increased Ca input to non-Mollisol cropland soils by 9-fold relative to preindustrial levels.
235 Alternatively, we can take the most recent available agricultural census liming data,³⁹ which are
236 from 1987, as a reference point. We estimate that agriculture has increased Ca inputs to Mollisol
237 cropland soils by 5-fold and non-Mollisol cropland soils by 16-fold based on 1987 liming rates
238 assuming that lime is 20% dolomite and 80% calcite.⁴⁰

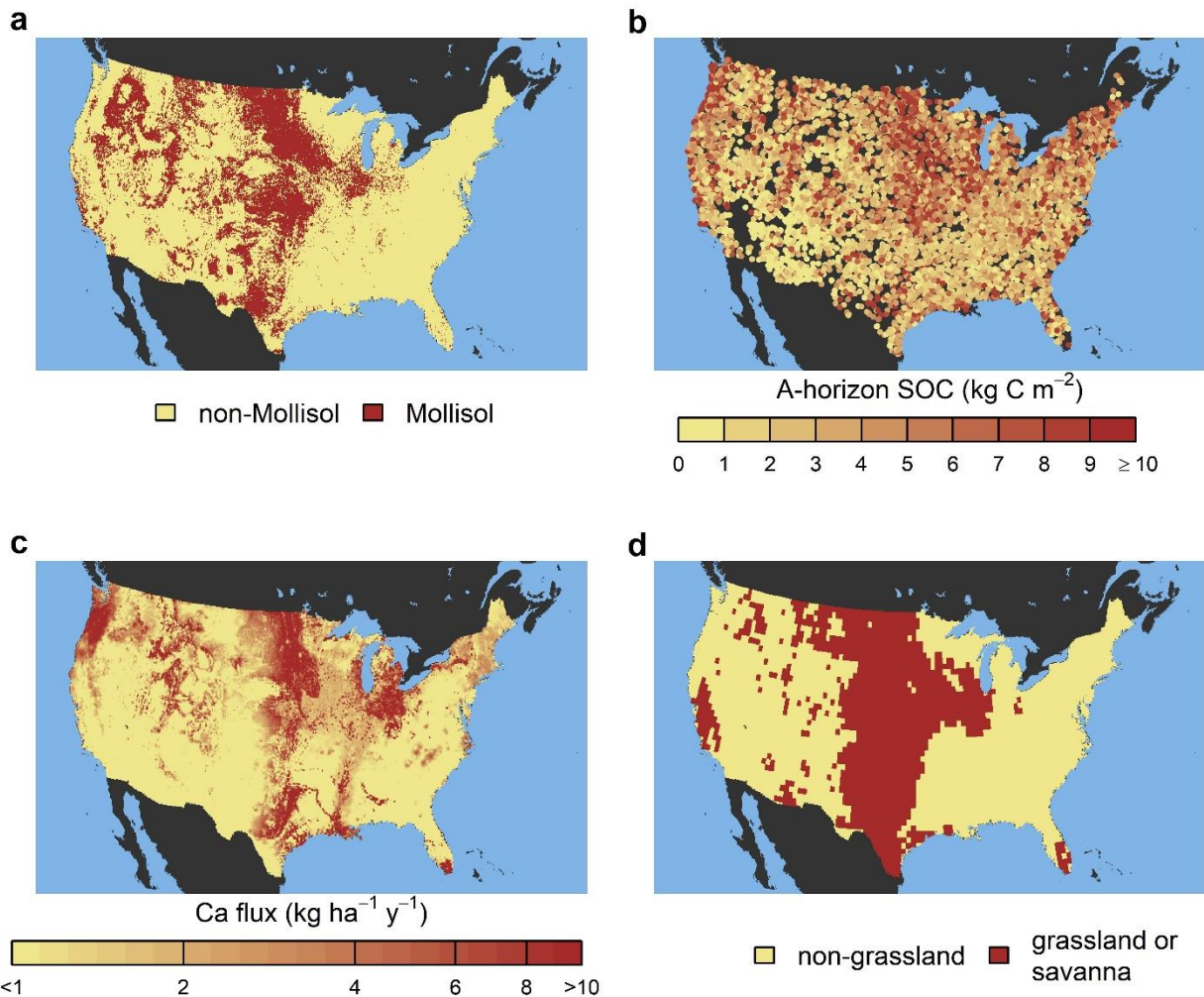
239 Clearly humans have dramatically altered the Ca cycle, and this has the potential to alter
240 carbon storage in Mollisols. Our finding that agriculture has accelerated dissolution of native
241 carbonates is consistent with other studies that have linked agricultural soil acidification to soil

242 inorganic carbon loss, although the acceleration of carbonate weathering predicted by our model
243 is modest compared to estimates in highly acidified systems (e.g., in China).⁴¹⁻⁴³ Our simulations
244 indicate that the more significant perturbation to the soil Ca cycle is agricultural lime addition.
245 Adoption of enhanced silicate⁴⁴ or carbonate⁴⁵ weathering for carbon dioxide removal will further
246 perturb the Ca cycle. These practices increase soil Ca inputs, which we have shown contribute to
247 Mollisol organic carbon storage over geologic timescales. However, increased Ca inputs have
248 occurred in response to unprecedented acid addition to cropland soils, and the effects of these
249 competing processes are hard to predict. For instance, experimental studies have found that the
250 effect of agricultural liming on soil organic carbon is not necessarily positive in the short term.⁴⁶
251 Similarly, enhanced silicate weathering does not necessarily benefit soil organic carbon storage in
252 the short term.⁴⁷ Liming may affect soil carbon differently than natural weathering because it is
253 intermittent: in the USA only 5-20% of cropland is limed in any given year.⁴⁸ Variable Ca
254 availability caused by intermittent liming may alternately stimulate and suppress decomposition,
255 with net effects that are challenging to predict.

256 In the broader context of conservation agriculture, our results suggest that farming practices
257 that mimic pre-agricultural vegetation in grasslands by increasing root inputs, increasing plant
258 diversity, or reducing tillage may not be sufficient to preserve Mollisol carbon. Instead, vegetation-
259 focused strategies may need to be complimented with geochemical strategies that mimic the
260 natural Ca cycle of these soils. For instance, reducing excess N can protect soil carbonates, which
261 reduces emissions from dissolution of soil inorganic carbon by strong acids,⁴³ while also
262 preserving a critical Ca reservoir that helps to protect soil organic carbon. In addition, changing
263 the cadence and quantity of lime applied to croplands could better simulate the natural weathering
264 regime. These efforts must be supported by collection of baseline statistics on the agricultural Ca

265 budget, which remains poorly quantified.⁴⁸ Closing these knowledge gaps is critical to managing
266 Earth's most fertile soils sustainably.

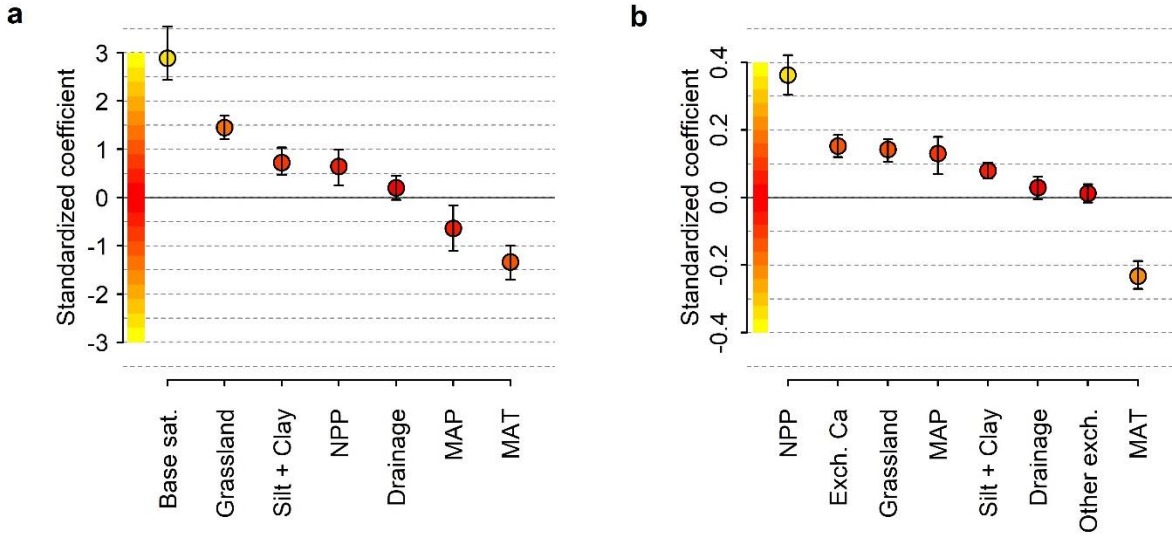
267



268

269 **Figure 1. Potential environmental controls on Mollisols across the USA.** (a) The distribution
 270 of the Mollisol soil order across the conterminous USA based on digital soil mapping.²¹ (b) Point
 271 observations of A-horizon soil organic carbon (SOC) derived from two databases.^{22,23} (c)
 272 Modeled preindustrial available calcium flux from silicate weathering, carbonate weathering, and
 273 atmospheric deposition. (d) The potential distribution of grasslands and savannas.²⁵

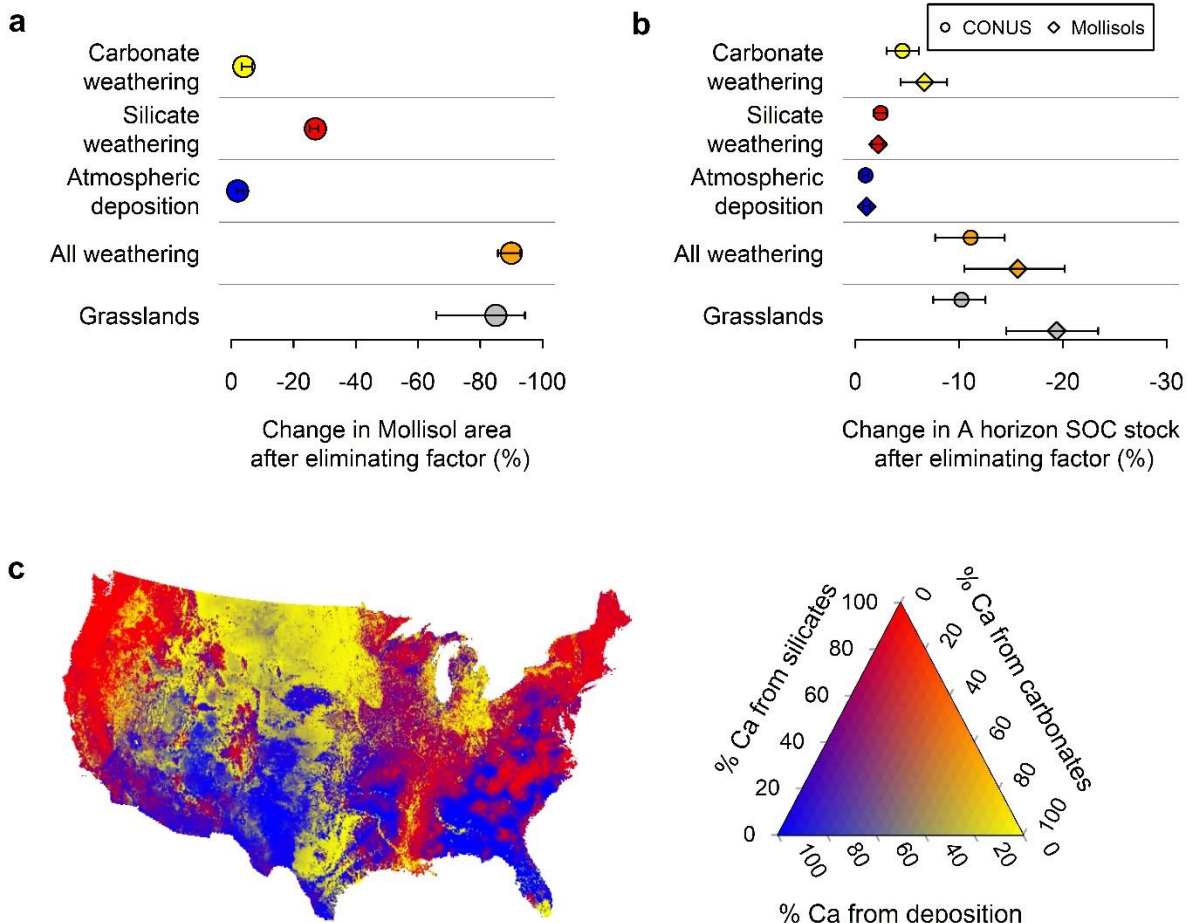
274



275

276 **Figure 2. Controls on Mollisol distribution and A-horizon soil organic carbon stocks in the**
 277 **USA. (a) Standardized regression coefficients derived from a multivariate logistic regression**
 278 **model, where the presence or absence of Mollisols was predicted as a function of the seven**
 279 **variables listed on the horizontal axis. (b) Standardized regression coefficients derived from a**
 280 **multivariate linear regression model, where A-horizon organic carbon stocks were predicted as a**
 281 **function of the eight variables listed on the horizontal axis. In both panels, whiskers show 95%**
 282 **confidence intervals derived from a spatial blocked bootstrapping procedure (see Methods).**
 283 **Standardization was performed by dividing each non-binary variable by two times the standard**
 284 **deviation.⁴⁹ The absolute value of each regression coefficient is an index of how strongly related**
 285 **each variable is to the response variable, and is shown with a relative color scale: yellow =**
 286 **maximum, red = zero. Abbreviations: Base sat. = base saturation, NPP = net primary**
 287 **productivity, MAT = mean annual temperature, MAP = mean annual precipitation, Exch. Ca =**
 288 **total exchangeable Ca, Other exch. = sum of non-Ca exchangeable ions.**

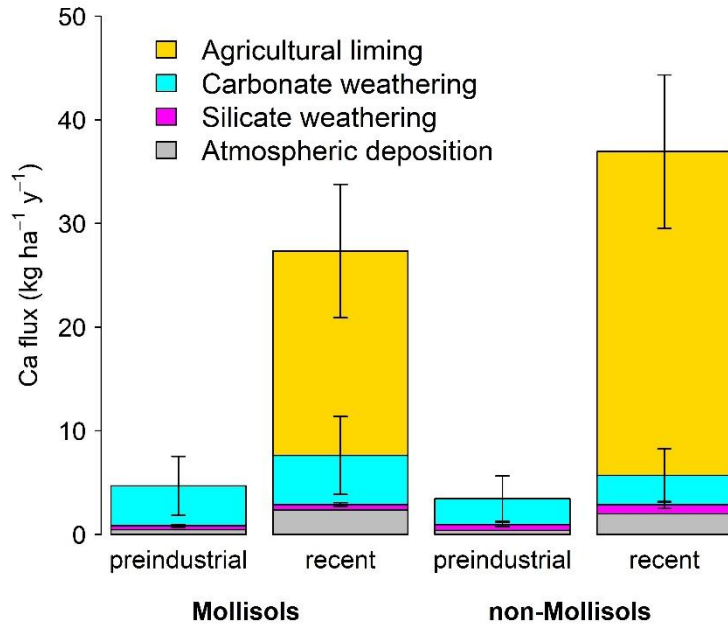
289



290

291 **Figure 3. Sources of available Ca and their effect on Mollisol extent across the USA.** (a) The
292 relative effect of removing Ca sources on predicted Mollisol area and the effect of eliminating
293 grasslands. (b) The relative effect of removing the same set of environmental factors on total A-
294 horizon soil organic carbon across the conterminous USA (CONUS; circles) and Mollisol areas
295 only (diamonds). Whiskers show 95% confidence intervals derived from spatial blocked
296 bootstrapping (see Methods). (c) The relative contributions of carbonate weathering, silicate
297 weathering, and atmospheric deposition to available Ca across the USA. Across all panels red =
298 silicate weathering, yellow = carbonate weathering, and blue = deposition.

299



300

301 **Figure 4. Modeled available Ca fluxes to croplands, preindustrial (1850) versus recent**
 302 **(2000-2010).** Stacked bars show the Ca sources: atmospheric deposition, carbonate weathering,
 303 silicate weathering, and agricultural liming. Data for Mollisol regions are shown on the left and
 304 non-Mollisol regions on the right. Whiskers show standard error estimates for each quantity
 305 derived from a Monte Carlo uncertainty analysis assuming +/- 20% variability in the model
 306 inputs and parameters. Liming estimates are based on the conservative assumption that farmers
 307 lime sufficiently to maintain soil pH (see Supplementary Information).

308

309 **Methods**

310 **Quantifying global role of Mollisols**

311 We calculated the total land area of Mollisols, the fraction of global agricultural production
312 occurring on Mollisols, and the fraction of agricultural soil organic carbon stored by Mollisols
313 using the Harmonized World Soil Database, Version 2.0 (HWSD).² For this analysis we assumed
314 that the distribution of Mollisols can be approximated by aggregating three World Reference
315 Base soil groups: Chernozems, Phaeozems, and Kastanozems.⁵⁰ HWSD soil mapping units were
316 assigned values based on the dominant soil type in each unit. Organic carbon storage in
317 croplands and Mollisols was calculated from the HWSD and summed to 1 m depth. We then
318 combined the HWSD with the 1 km resolution GFSAD 2010 croplands mask³ to estimate the
319 area of croplands and cropland organic carbon storage. Production of wheat, corn, and soy
320 occurring on Mollisols was obtained by combining the HWSD with SPAM global production
321 maps for 2010.⁵¹ Production values were rescaled to calories based on UN Food and Agriculture
322 Organization Annex I food composition tables.⁵²

323 **Geochemical model overview**

324 We developed a simplified geochemical model to simulate the release of Ca from silicate and
325 carbonate weathering in the top 1 m of soil across the USA. We parametrized the model with
326 existing data when possible and then calibrated remaining parameters related to mineral surface
327 reactivity so that modeled soil pH matched observed modern soil pH across the study region. We
328 based our model on existing geochemical models that were designed to simulate soil acid-base
329 chemistry in response to acid rain.⁵³ Our model also incidentally resembles approaches used to
330 simulate enhanced silicate weathering,⁵⁴ although it was not designed for this purpose and is less
331 complex. The model treated the entire upper 100 cm of soil as a single chemically homogeneous
332 reservoir, tracking the inputs and outputs of seven ions that control soil pH and weathering rates:

333 Ca^{2+} , Mg^{2+} , Na^+ , K^+ , SO_4^{2-} , NO_3^- , Cl^- . These ions were sourced from dissolution of silicate and
334 carbonate minerals, atmospheric deposition, agricultural inputs, and biological fixation in the
335 case of N. Ions were lost via leaching, carbonate mineral precipitation, export in crop biomass,
336 and volatilization in the case of N. Additional ions were assumed to equilibrate instantaneously
337 with the soil solution and hence were modeled implicitly as a function of other factors: H^+ , Al^{3+} ,
338 $\text{Al}(\text{OH})^{2+}$, $\text{Al}(\text{OH})_2^{+}$, $\text{AlH}_2\text{Org}^{2+}$, AlHOrg^+ , OH^- , CO_3^- , HCO_3^- , H_2Org^- , HOrg^{2-} , Org^{3-} , $\text{Al}(\text{OH})_4^-$.
339 We approximated ion activities with concentrations because under most conditions modeled
340 ionic strengths were too low to affect our results. Mineral concentrations were treated as constant
341 at the timescales being modeled. While the model was able to simulate year-to-year weathering
342 dynamics, for the purposes of this analysis, we applied a steady-state solution because this
343 simplified computations substantially. The model had nine governing equations: one for each of
344 the seven conserved ions and two algebraic constraints stipulating charge balance and
345 conservation of ions adsorbed on the soil exchange complex (Table S4). A full description of the
346 model is provided in the Supplementary Information file.

347 **Input data**

348 Whenever possible, we used spatially explicit environmental data to assign model parameters.
349 When applicable, we used time-averaged environmental parameters to drive the model, setting
350 the years 2001-2010 as our reference period for recent environmental conditions. To capture pre-
351 industrial conditions, we reset deposition rates for N and S, reset atmospheric pCO_2 , and turned
352 off the model's agricultural nutrient budget.

353 To parametrize climate and soil hydrologic properties, we used several sources. We
354 derived mean annual air temperature from PRISM 30-year normals (1991-2020) at an 800 m
355 resolution⁵⁵ and treated air temperature as a proxy for soil temperature when running the model.

356 We calculated recharge (RC) using the Global Streamflow Characteristics Database (GSCD),
357 which provides 0.125 degree resolution estimates of streamflow and base flow index.⁵⁶ We
358 calculated recharge by multiplying streamflow by the baseflow index. We constrained soil
359 moisture with the satellite-informed Global Land Evaporation Amsterdam Model (GLEAM)
360 V3.8 root zone soil moisture dataset (0.25 degree resolution).⁵⁷ We also obtained pedotransfer-
361 based maps of wilting point and field capacity from GLEAM. Finally, we parametrized net
362 primary productivity (NPP) using MOD17 (500 m resolution).⁵⁸

363 We parametrized soil mineralogy using two sources. For silicate minerals, we spatially
364 interpolated data from the North American Soil Geochemical Landscapes Project (NASGLP),²⁰
365 which includes estimates of major element abundance and quantitative X-ray diffraction data for
366 a selection of silicate and carbonate minerals. We used these data to directly constrain some
367 minerals and approximate concentrations of others that are not directly reported by NASGLP.
368 First, we averaged A-horizon and C-horizon data at the NASGLP sampling locations. We then
369 interpolated the NASGLP data for each mineral to locations where we ran the geochemical
370 model, using inverse distance weighting with an exponent of 2 and an averaging neighborhood
371 of 75 km. Plagioclase feldspar and the plagioclase anorthite fraction (fAn) were estimated by
372 first multiplying the molar concentration of Na from the NASGLP by the formula weight of
373 albite. Where albite exceeded 80% of the total plagioclase feldspar content obtained from the
374 NASGLP, albite was reset to 80% of the plagioclase content. Anorthite was then assumed to
375 make up the remainder of the plagioclase pool.²⁶ K-feldspar, hornblende, and pyroxene were
376 taken directly from the NASGLP X-ray diffraction estimates. To represent clay minerals, we
377 limited our analysis to chlorite (clinochlore) and illite (approximated as muscovite), which we
378 treated as generalized categories that stand in for the full diversity of Mg- and K-bearing 2:1

379 phyllosilicates (e.g. vermiculite and smectite group clays). Illite was calculated by subtracting
380 the K in K-feldspar from total K and assigning all residual K to illite. Similarly, chlorite was
381 calculated by first calculating the amount of Mg in hornblende, pyroxene, and dolomite (Table
382 S6). This value was subtracted from total Mg, and any residual Mg was assigned to chlorite.

383 To estimate carbonate mineral stocks, we did not use NASGLP data directly. Given the
384 high weatherability of carbonates, small quantities of carbonate mineral had a large effect on
385 modeled soil pH values; hence we used high-resolution digital soil maps from NATSGO²¹ to
386 ensure accurate assignment of soil carbonate content. We first calculated the stock of carbonate
387 in CaCO₃ equivalents to 1 meter depth from NATSGO. Next, we subdivided this stock into
388 calcite and dolomite components by using the data from the NASGLP to calculate the ratio of
389 calcite to dolomite. In addition to CaCO₃ content, we derived soil texture (silt, sand, and clay
390 percentages), cation exchange capacity, and soil bulk density parameters from NATSGO,
391 averaging these properties over the top 1 meter of soil or to bedrock if shallower than 1 meter.
392 All NATSGO soil properties were summarized by calculating the share-weighted average within
393 soil mapping units. Data were then extracted using the 30-meter resolution gridded version of
394 NATSGO.

395 We parametrized the cropland N inputs and outputs using a county-level nutrient budget
396 for the period 1987-2012.⁵⁹ We ran the geochemical model in one of two modes, either with
397 cropland nutrient imports and exports enabled or with only natural N fixation rates enabled. We
398 determine which mode to use by assigned modeled locations to cropland or non-cropland land
399 cover using the GFSAD 1 km cropland mask.³

400 We parameterized deposition of N, S, Cl, Ca, Mg, Na, and K, using gridded data from the
401 US Environmental Protection Agency's National Trend Network,⁶⁰ which we averaged for 2001-

402 2010. To represent preindustrial deposition of N and S, we used the multi-model average from
403 the ACCMIP project for the year 1850.²⁴ For Cl, Ca, Mg, Na, and K no data from before the year
404 2000 were available. Human activity has increased deposition of base cations, including Ca, in
405 the Western USA.³⁶ To account for this trend, we applied a factor of 5 difference between recent
406 and preindustrial times, which approximates dynamics recorded in lake sediment cores in
407 Colorado.³⁶ We applied this multiplier to Ca, Mg, and K, but left Na unchanged since this solute
408 is primarily derived from marine aerosols outside of deserts.

409 **Model calibration and uncertainty**

410 We implemented the model at point locations, extracting data from the aforementioned
411 environmental datasets at each point. For the calibration and validation steps, we selected points
412 by acquiring soil pH data from the USDA NRCS National Cooperative Soil Survey (NCSS)
413 Kellogg Soil Survey Laboratory database. We computed depth weighted average pH values in a
414 1:1 water matrix for all soil profiles with available data to a depth of 1 m, or to the depth of the
415 lowermost C horizon in cases where the profile terminated below 1 m. Similarly, we computed
416 depth-weighted average values for exchangeable cations using the NCSS database. We
417 represented Ca^{2+} , Mg^{2+} , Na^+ , and K^+ using NH_4 -acetate (pH 7) extraction data and Al^{3+} from KCl
418 extraction. Exchangeable H^+ was estimated by subtracting the sum of exchangeable Ca^{2+} , Mg^{2+} ,
419 Na^+ , K^+ , and Al^{3+} from the cation exchange capacity (CEC) obtained by the NH_4 -acetate method.
420 When the sum of these ions exceeded the CEC, exchangeable H^+ was set to zero and the values
421 of all ions were rescaled by the value (CEC / sum cations) so that the sum equaled the CEC.

422 We spatially resampled the pH and exchangeable cation data by binning them into 1
423 degree by 1 degree cells based on their latitude and longitude and then resampling 6,000
424 locations with replacement, with sampling weights inversely proportional to the number of

425 profiles in each cell. We extracted environmental data at these points and discarded those with
426 missing data, yielding 4,149 unique pH observations that were evenly distributed across the
427 conterminous USA (Figure S1). Exchangeable ions were only reported at 2,484 locations with
428 pH measurements. Because we resampled with replacement, some soil profiles occurred more
429 than once by design; the total number of pH observations was 5,389 (including pseudo-
430 replicates) and the total number of exchangeable cation observations was 3,280.

431 We calibrated the model by randomly sampling 2,000 training points from the NCSS
432 profiles and using them for model inversion based on soil pH. We optimized two parameters, r_2
433 and r_3 , which controlled the reactivity for secondary phyllosilicate minerals and carbonate
434 minerals respectively (see Supplementary Information). We calibrated the model using a Markov
435 Chain Monte Carlo (MCMC) approach, applying the adaptive Metropolis Hastings algorithm
436 with delayed rejection⁶¹ implemented via the R package FME.⁶² The cost function was defined to
437 minimize errors in soil pH. We initiated the MCMC algorithm with manually calibrated initial
438 parameter values and uninformative priors. The initial model variance was set equal to the mean
439 squared residuals based on the initial parameter estimates, and the initial jump values were set to
440 10% of the initial parameters. The adaptive stage of the algorithm was run for a burn-in period of
441 1,000 iterations updating the covariance matrix every 50 iterations with the number of delayed
442 rejections steps set to 2. After burn-in sampling continued for an additional 1,000 iterations. We
443 checked for convergence by running the algorithm using perturbed values of the starting
444 parameters and different training samples and found that results were comparable. The final
445 calibration yielded values of $10^{-6.8}$ for r_2 and $10^{-6.3}$ for r_3 .

446 We estimated uncertainty in modeled Ca fluxes using a Monte Carlo approach. We
447 expanded this analysis beyond the calibrated parameters to address uncertainty in all parameters,

448 excepting chemical formulae and well-known physical constants. Variables and parameters
449 included in the uncertainty analysis included: soil moisture, field capacity, wilting point,
450 recharge, net primary productivity, temperature, all deposition fluxes, all components of the
451 agricultural N budget, cation exchange capacity, sand, silt and clay fractions, bulk density, the
452 reaction order for silicate weathering, all mineral surface areas, all constants related to organic
453 acid equilibria, Q_{10} , decay rate, and input rate for DOC, the coefficient for gaseous loss of N,
454 weathering rate parameters r_1 , r_2 , and r_3 , and all cation exchange constants. Uncertainties for
455 most of these parameters could not be constrained. Instead, we applied a uniform relative
456 uncertainty distribution of +/- 20% to each variable or parameter. Specifically, we ran the model
457 at the 2,000 calibration points 1,000 times, randomly rescaling each parameter or environmental
458 input by a value between 80% and 120% of the observed value. We treated the standard
459 deviation of the Ca flux distributions derived from this process as a first-order estimate of
460 uncertainty given an assumed 20% range in all inputs.

461 **Statistical analysis**

462 After calibrating the geochemical model, we used it to create maps of preindustrial Ca pools and
463 fluxes across the conterminous USA. We used these maps to quantify the strength of the
464 relationships between occurrence of Mollisols, A-horizon organic carbon, and soil Ca availability
465 using logistic regression. To create the maps, we established a 10-kilometer resolution grid
466 across the study region and extracted environmental data at each point in the grid. Presence or
467 absence of Mollisols was obtained from NATSGO. For each NATSGO map unit, we identified
468 the soil order with the largest share (areal contribution), excluding non-soil land classes. When
469 modelling Mollisol extent, we represented soil Ca availability with the modern base saturation
470 percentage. Predicted Mollisol extents were obtained by applying a probability threshold to the

471 logistic regression output, with the threshold optimized so that predicted Mollisols land area
472 equaled the actual mapped area (probability = 0.4).

473 Following a similar protocol, we quantified the strength of the relationship between A-
474 horizon soil organic carbon (SOC) stocks from RaCA²² and the NCSS²³ databases and Ca using
475 ordinary least squares regression. When working with data from RaCA and NCSS, we calculated
476 the SOC stock in all horizons with the master designation “A”. The SOC stock (kg C m⁻²) was
477 calculated from the organic carbon percentage (OC%), the inorganic carbon percentage (IC%),
478 A-horizon thickness (TH, cm), rock fraction (RF, unitless) and bulk density (BD, g cm⁻³) as:

479 $\text{SOCstock} = ((\text{OC}\% - \text{IC}\%)/100) * \text{BD} * \text{TH} * (1 - \text{RF}) * 10$ (Equation 23)

480 Inorganic carbon was calculated from CaCO₃ equivalents reported in RaCA. In the few cases
481 where IC% exceeded OC%, OC% was set to zero. In the case of NCSS, we used the “estimated
482 organic C” field, which is already corrected for IC where applicable, or organic carbon content
483 estimated via the Walkley Black method when this field was not available. After calculating SOC
484 in each A horizon, we summed all A horizon stocks for each pedon to obtain total A-horizon
485 SOC. We log transformed A-horizon SOC stocks before fitting the model. When modelling A-
486 horizon SOC, we used modern total exchangeable calcium (ceq kg⁻¹), and also included the sum
487 of all other exchange ions as an additional predictor in the regression model.

488 In specifying both regression models, we included the presence of grassland vegetation as
489 a predictor using potential natural vegetation maps developed by ISCLP. We treated grassland
490 presence as a binary predictor, combining grasslands and savannas into a single category (present
491 = 1, absent = 0). In addition to vegetation, we controlled for mean annual temperature and mean
492 annual precipitation based on 30-year normals from Prism.⁵⁵ We also included three additional

493 potential confounding variables: the logarithm of average NPP, derived from MOD17 for the
494 period 2001-2010, average silt plus clay content of the top meter of soil, and soil drainage class.
495 The latter two variables were derived from NATSGO.²¹ Drainage class categories were assigned
496 numerical values from 1-7, with 1 being excessively drained and 7 being very poorly drained.
497 When fitting the regression model for SOC, we also included the sum of non-Ca exchangeable
498 ions (ceq kg^{-1}) as an additional predictor. We compared the relative importance of different
499 predictors in the regression models by standardizing all predictors upstream of fitting the models.
500 We standardized by dividing predictors by two times the standard deviation, which is
501 recommended in cases when some predictors are binary.⁴⁹

502 In addition to computing scaled coefficients, we evaluated the effect of specific Ca
503 sources on Mollisol extent and A-horizon SOC under preindustrial conditions. We evaluated the
504 effect of cation inputs from carbonate weathering and silicate weathering by running the model
505 with each mineral cation source eliminated, which meant that Ca, but also Mg, K, and Na fluxes
506 were affected by removing each source. We achieved this by re-setting the surface areas of all
507 silicates, all carbonates, or both mineral types to zero. In the case of deposition, we set base
508 cation deposition to zero. Each of these modified model runs generated predictions of
509 exchangeable Ca in the absence of each cation source; these values were then used as inputs to
510 the fitted regression models and used to predict either Mollisol extent or A-horizon SOC. We
511 also quantified the effect of eliminating grasslands by setting the ISCLP-derived grassland and
512 savanna predictor to zero everywhere and then obtaining predictions from the fitted regression
513 models.

514 We ran regressions on the full population of model evaluation points ($n = 77,115$ points
515 sampled from NATSGO; 11,332 A-horizon SOC estimates from RaCA and NCSS). We

516 addressed the spatial dependence of these observations by performing nonparametric spatially
517 blocked bootstrapping.²⁶ This involved dividing the data (NATSGO grid or RaCA/NCSS based)
518 into blocks defined by 2-by-2 degree grid cells and then resampling the cells with replacement
519 1,000 times. We fit a logistic or ordinary least squares regression to each of the 1,000 resampled
520 datasets and stored the regression coefficients. We then calculated bias corrected and accelerated
521 95% confidence intervals from the bootstrap replicates.⁶³ We followed the same protocol for
522 estimating uncertainty associated with predicted Mollisol areas and A-horizon SOC stocks after
523 resetting the model inputs as described above.

524 Soil organic matter can contribute to cation exchange capacity, which may explain a
525 relationship between total exchangeable calcium and SOC even in the absence of an effect of Ca
526 on SOC persistence. To account for this possibility, we conducted an additional regression
527 analysis after correcting total cation exchange capacity for the contribution of soil organic matter.
528 Corrected cation exchange capacity (CEC-c, ceq kg^{-1}) was obtained from the uncorrected CEC
529 and the soil organic matter percentage (SOM%) from NATSGO:

$$530 \quad \text{CEC-c} = \text{CEC} - \text{CEC-OM} * (\text{SOM\%}/100) \quad (\text{Equation 24})$$

531 Where CEC-OM is the cation exchange capacity of organic matter, assumed equal to 200 ceq kg^{-1}
532 ^{1.}⁶⁴ This formula could generate negative or zero values, and so in cases where CEC-c was less
533 than a minimum value of 0.01 we re-set it to this value. The results of the regressions computed
534 with CEC-c were similar to the primary results (Figure S5).

535 **Acknowledgements**

536 Work at LLNL and UCD was primarily supported by Laboratory Directed Research and
537 Development grant 22-ERD-19 under the auspices of the DOE, Contract DE-AC52-07NA27344.
538 Additional support for manuscript preparation was provided by the LLNL Lab Directed Research

539 and Development program (#24-SI-002), the DOE Office of Science ‘Terraforming Soil’ Carbon
540 Negative Energy Earthshot Research Center (SCW1841). We thank Oliver Chadwick for
541 feedback on early drafts of this manuscript and Claire Kouba and Iris Holzer for advice related to
542 model development.

543 **Author contributions:** Conceptualization: EWS, HRG, RL, KJM, JP, NS, DZ, KG;
544 Methodology: EWS, KG; Investigation: EWS; Visualization: EWS; Supervision: EWS, KG;
545 Writing—original draft: EWS; Writing—review & editing: EWS, HRG, RL, KJM, JP, NS, DZ,
546 KG

547 **Competing interests:** Authors declare that they have no competing interests.

548 **Data and materials availability:** Model code is available at [GitHub - eslessarev/Calcium-promotes-carbon-rich-grassland-soil-R-Code](https://github.com/eslessarev/Calcium-promotes-carbon-rich-grassland-soil-R-Code): Code associated with manuscript "Calcium promotes carbon-rich grassland soils"

551 **References**

- 552 1. Liu, X. *et al.* Overview of Mollisols in the world: Distribution, land use and management.
553 *Can. J. Soil. Sci.* **92**, 383–402 (2012).
- 554 2. *Harmonized World Soil Database Version 2.0.* (FAO; International Institute for Applied
555 Systems Analysis (IIASA);, 2023). doi:10.4060/cc3823en.
- 556 3. Teluguntla, P. *et al.* NASA Making Earth System Data Records for Use in Research
557 Environments (MEaSURES) Global Food Security Support Analysis Data (GFSAD) Crop
558 Mask 2010 Global 1 km V001. NASA Land Processes Distributed Active Archive Center
559 <https://doi.org/10.5067/MEASURES/GFSAD/GFSAD1KCM.001> (2016).

560 4. Thaler, E. A., Larsen, I. J. & Yu, Q. The extent of soil loss across the US Corn Belt. *Proc.*
561 *Natl. Acad. Sci. U.S.A.* **118**, e1922375118 (2021).

562 5. Boincean, B. & Dent, D. Potential of Chernozem to Increase Food Security and Mitigate
563 Global Warming. in *Farming the Black Earth* 189–204 (Springer International Publishing,
564 Cham, 2019). doi:10.1007/978-3-030-22533-9_8.

565 6. Dokuchaev, V. V. *The Russian Chernozem.* (1883).

566 7. Rasse, D. P., Rumpel, C. & Dignac, M.-F. Is soil carbon mostly root carbon? Mechanisms for
567 a specific stabilisation. *Plant Soil* **269**, 341–356 (2005).

568 8. Sokol, N. W., Kuebbing, Sara. E., Karlsen-Ayala, E. & Bradford, M. A. Evidence for the
569 primacy of living root inputs, not root or shoot litter, in forming soil organic carbon. *New*
570 *Phytol* **221**, 233–246 (2019).

571 9. Schmidt, M. W. I., Skjemstad, J. O. & Jäger, C. Carbon isotope geochemistry and
572 nanomorphology of soil black carbon: Black chernozemic soils in central Europe originate
573 from ancient biomass burning. *Global Biogeochemical Cycles* **16**, (2002).

574 10. Dreibrodt, S. *et al.* Earthworms, Darwin and prehistoric agriculture-Chernozem genesis
575 reconsidered. *Geoderma* **409**, 115607 (2022).

576 11. Lynch, J. P. & Wojciechowski, T. Opportunities and challenges in the subsoil: pathways to
577 deeper rooted crops. *Journal of Experimental Botany* **66**, 2199–2210 (2015).

578 12. Sprunger, C. D., Oates, L. G., Jackson, R. D. & Robertson, G. P. Plant community
579 composition influences fine root production and biomass allocation in perennial bioenergy
580 cropping systems of the upper Midwest, USA. *Biomass and Bioenergy* **105**, 248–258 (2017).

581 13. Smith, P. Soil carbon sequestration and biochar as negative emission technologies. *Glob*
582 *Change Biol* **22**, 1315–1324 (2016).

583 14. Shabtai, I. A. *et al.* Calcium promotes persistent soil organic matter by altering microbial
584 transformation of plant litter. *Nat Commun* **14**, 6609 (2023).

585 15. Rowley, M. C., Grand, S. & Verrecchia, É. P. Calcium-mediated stabilisation of soil organic
586 carbon. *Biogeochemistry* **137**, 27–49 (2018).

587 16. Rowley, M. C., Grand, S., Spangenberg, J. E. & Verrecchia, E. P. Evidence linking calcium
588 to increased organo-mineral association in soils. *Biogeochemistry* **153**, 223–241 (2021).

589 17. Rasmussen, C. *et al.* Beyond clay: towards an improved set of variables for predicting soil
590 organic matter content. *Biogeochemistry* **137**, 297–306 (2018).

591 18. von Fromm, S. F. *et al.* *Continental-Scale Controls on Soil Organic Carbon across Sub-*
592 *Saharan Africa*. <https://soil.copernicus.org/preprints/soil-2020-69/> (2020) doi:10.5194/soil-
593 2020-69.

594 19. Bockheim, J. G. Mollic Epipedon. in *Soil Geography of the USA* 29–46 (Springer
595 International Publishing, Cham, 2014). doi:10.1007/978-3-319-06668-4_5.

596 20. Smith, D. B. & Cannon, W. F. Geochemical and Mineralogical Data for Soils of the
597 Conterminous United States.

598 21. Soil Survey Staff. Gridded National Soil Survey Geographic (gNATSGO) Database for the
599 Conterminous United States.

600 22. Wills, S. *et al.* Overview of the U.S. Rapid Carbon Assessment Project: Sampling Design,
601 Initial Summary and Uncertainty Estimates. in *Soil Carbon* (eds Hartemink, A. E. &
602 McSweeney, K.) 95–104 (Springer International Publishing, Cham, 2014). doi:10.1007/978-
603 3-319-04084-4_10.

604 23. National Cooperative Soil Survey. National Cooperative Soil Survey Soil Characterization
605 Database. (2018).

606 24. Lamarque, J.-F. *et al.* Multi-model mean nitrogen and sulfur deposition from the
607 Atmospheric Chemistry and Climate Model Intercomparison Project (ACCMIP): evaluation
608 of historical and projected future changes. *Atmos. Chem. Phys.* **13**, 7997–8018 (2013).

609 25. RAMANKUTTY, N. & FOLEY, J. A. ISLSCP II Potential Natural Vegetation Cover.
610 1.72082 MB Preprint at <https://doi.org/10.3334/ORNLDAA/961> (2010).

611 26. Slessarev, E. W., Chadwick, O. A., Sokol, N. W., Nuccio, E. E. & Pett-Ridge, J. Rock
612 weathering controls the potential for soil carbon storage at a continental scale.
613 *Biogeochemistry* **157**, 1–13 (2022).

614 27. Ratajczak, Z., Nippert, J. B., Briggs, J. M. & Blair, J. M. Fire dynamics distinguish
615 grasslands, shrublands and woodlands as alternative attractors in the C entral G reat P lains
616 of N orth A merica. *Journal of Ecology* **102**, 1374–1385 (2014).

617 28. Staver, A. C., Archibald, S. & Levin, S. Tree cover in sub-Saharan Africa: Rainfall and fire
618 constrain forest and savanna as alternative stable states. *Ecology* **92**, 1063–1072 (2011).

619 29. FAO/UNESCO. FAO Soil map of the world. (1974).

620 30. Slessarev, E. W. *et al.* Water balance creates a threshold in soil pH at the global scale. *Nature*
621 **540**, 567–569 (2016).

622 31. Slessarev, E. W., Feng, X., Bingham, N. L. & Chadwick, O. A. Landscape Age as a Major
623 Control on the Geography of Soil Weathering. *Global Biogeochem. Cycles* **33**, 1513–1531
624 (2019).

625 32. Bockheim, J. G. *Soils of the Laurentian Great Lakes, USA and Canada*. (Springer
626 International Publishing, Cham, 2021). doi:10.1007/978-3-030-52425-8.

627 33. Jacobs, P. M. & Mason, J. A. Impact of Holocene dust aggradation on A horizon
628 characteristics and carbon storage in loess-derived Mollisols of the Great Plains, USA.
629 *Geoderma* **125**, 95–106 (2005).

630 34. Cooke, M. J., Stern, L. A., Banner, J. L. & Mack, L. E. Evidence for the silicate source of
631 relict soils on the Edwards Plateau, central Texas. *Quat. res.* **67**, 275–285 (2007).

632 35. Capo, R. C. & Chadwick, O. A. Sources of strontium and calcium in desert soil and calcrete.
633 *Earth and Planetary Science Letters* **170**, 61–72 (1999).

634 36. Neff, J. C. *et al.* Increasing eolian dust deposition in the western United States linked to
635 human activity. *Nature Geosci* **1**, 189–195 (2008).

636 37. Albani, S. *et al.* Paleodust variability since the Last Glacial Maximum and implications for
637 iron inputs to the ocean. *Geophysical Research Letters* **43**, 3944–3954 (2016).

638 38. Muhs, D. R. & Bettis, E. A. Geochemical Variations in Peoria Loess of Western Iowa
639 Indicate Paleowinds of Midcontinental North America during Last Glaciation. *Quat. res.* **53**,
640 49–61 (2000).

641 39. Haines, M., Fishback, P. & Rhode, P. United States Agriculture Data, 1840 - 2012: Version 4.
642 ICPSR - Interuniversity Consortium for Political and Social Research
643 <https://doi.org/10.3886/ICPSR35206.V4> (2014).

644 40. West, T. O. & McBride, A. C. The contribution of agricultural lime to carbon dioxide
645 emissions in the United States: dissolution, transport, and net emissions. *Agriculture,*
646 *Ecosystems & Environment* **108**, 145–154 (2005).

647 41. Kim, J. H., Jobbág, E. G., Richter, D. D., Trumbore, S. E. & Jackson, R. B. Agricultural
648 acceleration of soil carbonate weathering. *Glob. Change Biol.* **26**, 5988–6002 (2020).

649 42. Raza, S. *et al.* Dramatic loss of inorganic carbon by nitrogen-induced soil acidification in
650 Chinese croplands. *Global Change Biology* **26**, 3738–3751 (2020).

651 43. Zamanian, K., Zarebanadkouki, M. & Kuzyakov, Y. Nitrogen fertilization raises CO₂ efflux
652 from inorganic carbon: A global assessment. *Global Change Biology* **24**, 2810–2817 (2018).

653 44. Taylor, L. L. *et al.* Enhanced weathering strategies for stabilizing climate and averting ocean
654 acidification. *Nature Clim Change* **6**, 402–406 (2016).

655 45. Liu, Z. *et al.* Large and active CO₂ uptake by coupled carbonate weathering. *Earth-Science
656 Reviews* **182**, 42–49 (2018).

657 46. Paradelo, R., Virto, I. & Chenu, C. Net effect of liming on soil organic carbon stocks: A
658 review. *Agriculture, Ecosystems & Environment* **202**, 98–107 (2015).

659 47. Sokol, N. W. *et al.* Reduced accrual of mineral-associated organic matter after two years of
660 enhanced rock weathering in cropland soils, though no net losses of soil organic carbon.
661 *Biogeochemistry* **167**, 989–1005 (2024).

662 48. Tsao, S. S.-E. *et al.* A spatially explicit dataset of agriculture liming across the contiguous
663 United States. Preprint at <https://doi.org/10.5194/essd-2025-411> (2025).

664 49. Gelman, A. Scaling regression inputs by dividing by two standard deviations. *Statistics in
665 Medicine* **27**, 2865–2873 (2008).

666 50. Labaz, B., Hartemink, A. E., Zhang, Y., Stevenson, A. & Kabała, C. Organic carbon in
667 Mollisols of the world – A review. *Geoderma* **447**, 116937 (2024).

668 51. Yu, Q. *et al.* A cultivated planet in 2010 – Part 2: The global gridded agricultural-production
669 maps. *Earth Syst. Sci. Data* **12**, 3545–3572 (2020).

670 52. FAO. Annex I: Food Composition Tables.

671 53. Bonten, L. T. C., Reinds, G. J. & Posch, M. A model to calculate effects of atmospheric
672 deposition on soil acidification, eutrophication and carbon sequestration. *Environmental*
673 *Modelling & Software* **79**, 75–84 (2016).

674 54. Bertagni, M. B., Calabrese, S., Cipolla, G., Noto, L. V. & Porporato, A. Advancing Enhanced
675 Weathering Modeling in Soils: Critical Comparison With Experimental Data. *J Adv Model*
676 *Earth Syst* **17**, e2024MS004224 (2025).

677 55. Prism Climate Group, Oregon State University. Prism climate data. (2011).

678 56. Beck, H. E., De Roo, A. & Van Dijk, A. I. J. M. Global Maps of Streamflow Characteristics
679 Based on Observations from Several Thousand Catchments*. *Journal of Hydrometeorology*
680 **16**, 1478–1501 (2015).

681 57. Martens, B. *et al.* GLEAM v3: satellite-based land evaporation and root-zone soil moisture.
682 *Geosci. Model Dev.* **10**, 1903–1925 (2017).

683 58. Zhao, M., Running, S., Heinsch, F. A. & Nemani, R. MODIS-Derived Terrestrial Primary
684 Production. in *Land Remote Sensing and Global Environmental Change* (eds Ramachandran,
685 B., Justice, C. O. & Abrams, M. J.) vol. 11 635–660 (Springer New York, New York, NY,
686 2010).

687 59. Swaney, D. P., Howarth, R. W. & Hong, B. Nitrogen use efficiency and crop production:
688 Patterns of regional variation in the United States, 1987–2012. *Science of The Total*
689 *Environment* **635**, (2018).

690 60. Schwede, D. B. & Lear, G. G. A novel hybrid approach for estimating total deposition in the
691 United States. *Atmospheric Environment* **92**, 207–220 (2014).

692 61. Haario, H., Laine, M., Mira, A. & Saksman, E. DRAM: Efficient adaptive MCMC. *Stat*
693 *Comput* **16**, 339–354 (2006).

694 62. Soetaert, K. & Petzoldt, T. Inverse Modelling, Sensitivity and Monte Carlo Analysis in *R*
695 Using Package **FME**. *J. Stat. Soft.* **33**, (2010).

696 63. DiCiccio, T. J. & Efron, B. Bootstrap confidence intervals. *Statist. Sci.* **11**, (1996).

697 64. Brady, N. C. & Weil, R. R. *The Nature and Properties of Soils*. (Pearson, Harlow, England
698 London New York, 2016).

699

700

701 **Supplemental Information: Calcium promotes carbon-rich grassland soils**

702 Slessarev, E.W.,^{1,2*} Goertzen, H.R.,³ Lybrand, R.,³ McFarlane, K.J.,⁴ Pett-Ridge, J.^{4,5,6}, Sokol,
703 N.⁴, Zaharescu, D.³ Georgiou, K.,⁷

704
705 ¹ Department of Ecology and Evolutionary Biology, Yale University, New Haven, CT, USA
706 ² Yale Center for Natural Carbon Capture, Yale University, New Haven, CT, USA³ Department

707 of Biological and Ecological Engineering, Oregon State University, Corvallis, OR, USA
708 ³ Department of Land Air and Water Resources, University of California, Davis, CA, USA
709 ⁴ Physical and Life Sciences Directorate, Lawrence Livermore National Laboratory, Livermore,
710 CA, USA

711 ⁵ Innovative Genomics Institute, University of California Berkeley, Berkeley, CA.
712 ⁶ Life & Environmental Sciences Department, University of California Merced, Merced, CA.
713 ⁷ Department of Biological and Ecological Engineering, Oregon State University, Corvallis, OR,
714 USA

715
716 *Corresponding author: eric.slessarev@yale.edu

717

718 **Contents:**

719 1) Supplemental Text: Geochemical model description
720 2) Figures S1 – S5
721 3) Tables S1 – S7
722 4) References

723 Supplemental Text: Geochemical model description

724 Governing equations

725 Our model was specified to track inputs and outputs of seven ions that control soil pH and
726 weathering rates: Ca^{2+} , Mg^{2+} , Na^+ , K^+ , SO_4^{2-} , NO_3^- , Cl^- (Table S3). These ions were sourced from
727 dissolution of silicate and carbonate minerals, atmospheric deposition, agricultural inputs, and
728 biological fixation in the case of N. Ions were lost via leaching, carbonate mineral precipitation,
729 export in crop biomass, and volatilization in the case of N. Additional ions were assumed to
730 equilibrate instantaneously with the soil solution and hence were modeled implicitly as a
731 function of other factors: H^+ , Al^{3+} , $\text{Al}(\text{OH})^{2+}$, $\text{Al}(\text{OH})_2^+$, $\text{AlH}_2\text{Org}^{2+}$, AlHOrg^+ , OH^- , CO_3^{2-} , HCO_3^- ,
732 H_2Org^- , HOrg^{2-} , Org^{3-} , $\text{Al}(\text{OH})_4^-$.

733 Hydrology

We parametrized leaching rates for major ions as a function of recharge or hydrologic baseflow (RC, mm y^{-1}), which we assume represents the flux of water that infiltrates the soil without being lost to evapotranspiration or overland flow. We partitioned the total amount of soil water (V , l) into mobile and immobile components, under the assumption that only a fraction of the soil pores are leached during leaching events. The immobile component of the soil water was equal to the water content at wilting point (V_{wp} , l), which governed the fraction of soil water mobilized during recharge:

$$741 \quad F_{mob} = (V - V_{wp})/V \quad (\text{Equation 1})$$

742 We assumed that only the solutes in the mobile fraction are vulnerable to leaching loss and that
743 solutes are partitioned into mobile and immobile fractions by F_{mob} . We also assumed that solutes
744 in the mobile fraction are conservatively diluted at the timescale of recharge events. The

745 concentration of solute i leached during recharge events (C_i) was therefore a function of the soil
746 moisture at field capacity, V_{fc} :

747 $C_i = M_i * F_{mob} / (V_{fc} - V_{wp})$ (Equation 2)

748 Where M_i was the total moles of the solute in the soil. The leaching rate for a given ion, L_i (mol
749 y^{-1}) was a function of concentration in recharge water (mol l^{-1}) times recharge ($l y^{-1}$):

750 $L_i = R C * C_i$ (Equation 3)

751 **Weathering kinetics**

752 Weathering kinetic expressions vary widely in complexity. We adopted a simple power law
753 description for silicate weathering kinetics. More complex approaches, such as transition state
754 theory, incorporate multiple reaction mechanisms. These approaches are sensitive to assumptions
755 regarding the type and reactivity of secondary minerals and the extent of mineral surface
756 passivation, which we could not parametrize at the scale of the USA. To further reduce
757 complexity, dissolution kinetics of tectosilicates and inosilicates were referenced to the reactivity
758 of plagioclase feldspar based on a compilation of field-based weathering rate measurements.¹

759 This was not possible for pyroxene given a lack of field based weathering rate estimates, so we
760 assigned this mineral a reaction rate of 1.0 relative to plagioclase. For tecto- or inosilicate
761 mineral i , weathering rates in the top 100 cm of soil (mol y^{-1}) were a function of total geometric
762 surface area (A_i , m^2), a reaction rate coefficient (r_i , mol $m^{-2} y^{-1}$), the ratio giving reaction rate
763 relative to plagioclase (RR_i , unitless), an Arrhenius-type term governing temperature dependence
764 (T_f , unitless), volumetric water content (θ $m^3 m^{-3}$), the hydrogen ion concentration ($[H^+]$), a
765 reference hydrogen ion concentration ($[H^+ r]$, set equal to 10^{-5}), and the reaction order with
766 respect to H^+ (n).

767 $W_i = A_i * r_1 * R R_i * T_f * \theta * (H^+ / H^+_{ref})^n$ (Equation 4)

768 For phyllosilicate minerals, the rate expression was identical except that the term $R R_i$ was
769 omitted and an affinity term was added to make the reactions reversible, allowing clay synthesis.

770 $W_{i, phyllo} = A_i * r_2 * T_f * \theta * (H^+ / H^+_{ref})^n * (1 - \Omega_i)$ (Equation 5)

771 The term r_2 gives a reaction rate coefficient for phyllosilicates. The parameter Ω_i was the
772 saturation index for phyllosilicate mineral i , where $\Omega_i = IAP_i / K_{sp}$. The IAP was the ion activity
773 product or reaction quotient. K_{sp} was the solubility constant for each mineral.

774 We assumed that the temperature and pH dependence of silicate weathering was the same
775 for all minerals. The activation energy for silicate weathering was set to equal 74 kJ mol⁻¹ K⁻¹.^[2]
776 The temperature modifier for silicate weathering was given by the following equation:

777 $T_f = \exp(-E_{asil}/R * (1/(T) - 1/(T_{ref})))$ (Equation 6)

778 Where E_{asil} was the activation energy for silicates, R was the universal gas constant, T was the
779 soil temperature approximated as the mean annual air temperature (K) and T_{ref} was a reference
780 temperature (298 K).

781 We assigned several silicate weathering parameters manually in order to match published
782 compilations of field weathering rates.^{3,4} The parameter r_1 represented the bulk plagioclase
783 feldspar weathering rate coefficient (y^{-1}) at a reference pH of 5.0 ($H_{ref} = 10^{-5}$). We assumed that
784 under the wettest climate conditions, mean soil pH approaches a value of 5.0,⁵ and so bulk
785 feldspar weathering rates ought to approach r_1 under these conditions. Across our calibration
786 dataset, the 95th percentile value for recharge (RC) equaled 474 mm, which implies that r_1 equals
787 $10^{-4.3}$ based on the power law relationship between recharge and bulk weathering rates reported

788 by Yu and Hunt (2018).⁴ Based on similar reasoning, we set the reaction order for H^+ , n , equal to
789 0.66. We chose this value because field estimates of silicate weathering rates increase by roughly
790 two orders of magnitude in the transition from dry conditions (infiltration rates $\sim 0.1 \text{ m y}^{-1}$) to
791 humid conditions (infiltration rates $\sim 1 \text{ m y}^{-1}$),³ and soil pH spans roughly 3 units in the transition
792 from wet to dry climates.⁵ This implies that weathering rates should increase by two orders of
793 magnitude over a three order of magnitude range in pH (reaction order = 0.66). This value is
794 reasonable for many silicates,⁶ and allowed us to recover the observed relationship between
795 feldspar weathering rates in the field and infiltration reasonably well with the calibrated model
796 (Figure S4).

797 We modeled carbonate weathering kinetics using a more complex expression based on
798 transition state theory because carbonate minerals dissolve and precipitate congruently in soil,
799 reducing uncertainty regarding secondary minerals and surface passivation. Dissolution and
800 precipitation for carbonate minerals was governed by the following equation:

801 $W_i, \text{carb} = A_i * r_3 * \theta * (R_{\text{acid}} * [H^+]^{nH} + R_{\text{neutral}} + R_{\text{CO}_2} * p\text{CO}_2^{n\text{CO}_2}) * (1 - \Omega_i)$ (Equation 7)

802 Where A_i was the total surface area for mineral i , r_3 was ratio of reactive surface area to
803 geometric surface area for carbonates, R_{acid} , R_{neutral} , and R_{CO_2} were separate reaction mechanisms
804 for acid, neutral, and CO_2 driven dissolution reactions, nH was the reaction order for H^+ , and
805 $n\text{CO}_2$ was the reaction order for CO_2 . The parameter Ω_i was the saturation index for carbonate
806 mineral i , where $\Omega_i = \text{IAP}_i / K_{\text{sp}}$. The IAP was the ion activity product or reaction quotient. K_{sp}
807 was the solubility constant for each mineral. Reaction mechanisms (R_m) were governed by
808 equations with the form:

809 $R_m = A_m * \exp(-Ea_m / R * (1 / (T) - 1 / (T_{\text{ref}})))$ (Equation 8)

810 Where A_m and Ea_m were the preexponential factor ($\text{mol m}^{-2} \text{ y}$) and activation energy ($\text{kJ mol}^{-1} \text{ K}^{-1}$) for mechanism m.

812 All spatially invariant parameters related to weathering reactions are given in Table S5.

813 Our treatment of weathering kinetics left two unknown parameters: r_2 , the reaction rate
814 coefficient for phyllosilicates, and r_3 , the ratio of reactive to total surface area for carbonates.

815 These parameters were obtained by model inversion (see Methods in main article).

816 **Mineral surface areas**

817 We estimated geometric surface areas for each mineral. For tectosilicates, inosilicates, and
818 carbonates, we assumed that particles were silt- and sand-sized and spherical. We calculated
819 surface area to volume ratios (SVR, $\text{m}^2 \text{ m}^{-3}$) for silt and sand:

820 $\text{SVR} = (4 * \pi * (D/2)^2) / (4/3 * \pi * (D/2)^3)$ (Equation 9)

821 Where D was the particle diameter, which we set to the geometric mean of each size class.⁷ The
822 average surface area to volume ratio for minerals in the silt and sand fraction was then calculated
823 as a weighted average based on silt and sand percentages derived from the NATSGO database
824 (see below). Clays (illite and chlorite) were modeled as cylindrical plates with a diameter of 1
825 μm and a diameter to height ratio of 10:1 [⁷]

826 $\text{SVR}_{\text{clay}} = ((D/10 * 2 * \pi * D/2) + (2 * \pi * (D/2)^2)) / ((D/10) * (\pi * (D/2)^2))$ (Equation 10)

827 Total geometric surface area for each mineral was obtained by multiplying the surface area to
828 volume ratio by the total volume of each mineral in the soil.

829 $A_i = \text{SVR}_i * P_i * (\rho_s / \rho_i) * h * 10^{-5}$ (Equation 11)

830 Where P_i was the percentage of mineral i in the soil, ρ_s was the bulk density of the soil, ρ_i was
831 the density of mineral i , and h was the soil thickness in mm. Chemical formulas and densities for
832 the minerals that we included in the model are shown in Table S6. For clay minerals, we limited
833 our analysis to chlorite (clinochlore) and illite (approximated as muscovite), which we treated as
834 generalized categories that stand in for the full diversity of Mg- and K-bearing 2:1 phyllosilicates
835 (e.g. vermiculite and smectite group clays).

836 **Equilibrium chemistry**

837 We parametrized a set of major equilibrium reactions that governed carbonate ion speciation,
838 aluminum hydrolysis, organic acid speciation, Al-organo ion pair formation, and cation exchange
839 reactions (Table S7). When possible, we obtained equilibrium constants by calculating them
840 from standard enthalpies and entropies, which we obtained from the SUPCRT92 thermodynamic
841 database⁸ loaded with the R package CHNOSZ.⁹

842 Carbonate equilibria depended on the average soil $p\text{CO}_2$, which we parametrized as a
843 function of soil respiration:¹⁰

844 $p\text{CO}_2 = p\text{CO}_{2\text{atm}} + 1.03 * R_s / T^2$ (Equation 12)

845 Where $p\text{CO}_{2\text{atm}}$ was atmospheric $p\text{CO}_2$, set to 380 ppm for 2001-2010^[11] and 280 ppm for
846 preindustrial times,¹² and R_s was soil respiration in $\text{g m}^{-2} \text{y}^{-1}$. We obtained R_s from net primary
847 productivity (NPP, $\text{g m}^{-2} \text{y}^{-1}$):¹³

848 $R_s = 1.24 * \text{NPP} + 24.5$ (Equation 13)

849 We modeled dissolution and precipitation of carbonates and phyllosilicates as reversible
850 processes governed by chemical equilibria (Table S7), which defined the saturation index (Ω)
851 used in weathering rate calculations. In the case of phyllosilicates, the saturation state depended

852 on dissolved H_4SiO_2 , which we did not model explicitly as a state variable. Instead, the
853 concentration of H_4SiO_2 was assumed to be determined by instantaneous dissolution and
854 precipitation of secondary amorphous SiO_2 (Table S7).

855 We represented organic acid speciation using the triprotic model and allowed for
856 formation of ion pairs between Al^{3+} and organic acids. Equilibrium constants for these reactions
857 were obtained by averaging published values from New England lakes, streams, and soils.¹⁴ To
858 parametrize equilibrium reactions involving organic acids, we estimated the amount of dissolved
859 organic carbon and then calculated total organic acid charge (Org_{tot} , moles charge) from total
860 DOC (moles). We converted DOC to Org_{tot} based on a charge density ($m = 0.049 \text{ mol mol}^{-1}$)
861 averaged from the New England water survey.¹⁴ We approximated soil DOC concentrations by
862 assuming that DOC inputs are equal to NPP, reasoning that over the long run all plant inputs to
863 soil must be converted to DOC before they are respired or sequestered. We then assumed that
864 DOC decays as a first order process and is lost due to leaching:

865 $d\text{DOC}/dt = \text{NPP} - k_{\text{DOC}} * Q_{10}^{((T - 293)/10)} * \text{DOC} - \text{DOC} * \text{RC} * F_{\text{mob}} / (V_{\text{fc}} - V_{\text{wp}})$ (Equation 14)

866 Where k_{DOC} was a decay constant and Q_{10} defined the temperature dependence of DOC decay.
867 We obtained k_{DOC} by taking the geometric mean of previously reported “fast” and “slow” DOC
868 decay constants.¹⁵ Assuming that DOC is maintained at steady state for our purposes, the organic
869 acid concentration (mol c l^{-1}) was obtained from the following equation:

870 $\text{Org}_{\text{tot}} = m * (\text{NPP}/12.01) / (1 + k_{\text{DOC}} * Q_{10}^{((T - 293)/10)}) * (1/V)$ (Equation 15)

871 Exchange reactions were specified using the Gaines-Thomas approach. We parameterized
872 cation exchange reactions using an existing compilation,¹⁶ which summarized Gaines-Thomas
873 exchange constants for sand, loess (silt enriched), and clay dominated soils in the Netherlands.

874 As a first order approximation, we assigned exchange constants by calculating the weighted
875 mean of the profile-averaged constants listed in the compilation, with weights given by the sand,
876 silt, and clay fractions obtained from NATSGO.

877 When calibrating the model, we simulated re-equilibration of soil pH with laboratory
878 conditions because in-situ pH and laboratory-measured pH can vary substantially.¹⁷ To do this,
879 we fixed soil water content so that the soil mass to water ratio equaled 1:1, set the temperature to
880 20°C, and adjusted pCO₂ to reflect the ambient atmospheric concentration. Concentrations of
881 conserved ions were adjusted to reflect the change in soil water content during measurement.
882 Charge balance and exchange reactions were solved based on laboratory parameters to yield
883 laboratory pH. In cases where the soil contained calcite, we assumed that calcite could partially
884 buffer pH at the timescale of laboratory measurement. This assumption is supported by a global
885 pH compilation, which shows that pH approximates a calcite-buffered value when carbonates are
886 present in even small amounts.⁵ To represent carbonate buffering in the lab, we fixed the
887 saturation index for calcite so that it would equal its value in the field and then solved for the
888 equilibrium Ca concentration at the laboratory pCO₂ and temperature.

889 **Nutrient budgets**

890 While our main goal was to model pre-agricultural Ca weathering across the USA, we
891 considered nutrient inputs and outputs in modern croplands to assist with model calibration and
892 to help us understand how Ca fluxes have changed over time. Nitrogen had the most complex
893 nutrient budget. To simplify N accounting, we assumed that all reduced N is completely nitrified
894 following DON export; hence all N is treated as NO₃⁻.¹⁸ In natural systems, the only N inputs in
895 the model were atmospheric deposition and nitrogen fixation (F_N, mol m⁻² y⁻¹), which we
896 modeled as a function of NPP.¹⁹

897 $F_N = 1.8 * (1 - \exp(-0.003 * NPP)) / 14.01$ (Equation 16)

898 In addition to leaching of NO_3^- , we considered leaching of organic N, which we assume happens
899 before nitrification. We assigned a molar CN ratio of 20, which is typical for dissolved organic
900 matter,²⁰ and modeled DON export as a function of DOC leaching:

901 $L_N = N * RC * F_{mob} / (V_{fc} - V_{wp}) + \text{DOC/CN}_{DOM} * RC * F_{mob} / (V_{fc} - V_{wp})$ (Equation 17)

902 Because we fixed the CN ratio for DOM, DON export could exceed inputs, leading to negative
903 NO_3^- concentrations. In these cases, we forced DON export to equal inputs and NO_3^-
904 concentrations equaled zero.

905 In croplands, we considered N inputs from fertilizer, manure, crop N fixation, free living
906 N fixation, and N removal in crop biomass:

907 $C_N = N_{fert} + N_{man} + N_{fix,crop} + N_{fix,free} - N_{rem}$ (Equation 18)

908 The first three of these parameters as well as the N removal rate varied spatially and were taken
909 from a published county-level compilation²¹ whereas free-living N fixation rates were
910 approximated at $0.036 \text{ mol m}^{-2} \text{ y}^{-1}$ ^[22] and did not vary spatially. The parameter N_{man} was set
911 equal to 20% of total manure N to account for inefficiency in manure recovery.²³

912 Nitrogen can be lost from soil via ammonia volatilization, NO_x emission, and
913 denitrification to N_2O or N_2 . The processes governing these fluxes are complex and representing
914 them in detail was beyond the scope of our effort. Instead, we manually calibrated a single
915 parameter, r_v , that controlled the N volatilization rate:

916 $V_N = N / N_{inputs} * r_v$ (Equation 19)

917 The expression was based on the assumption that N volatilization is proportional to the total
918 available N pool but inversely proportional to N inputs. We reasoned that as N inputs increase,
919 the opportunity for denitrification and ammonia volatilization would be lower because more N
920 would escape the soil before volatilization. This is consistent with the observation that low-input
921 ecosystems volatilize a greater fraction of N than high-input agricultural systems.²⁴ We selected a
922 value of 0.3 y^{-1} for r_v , which ensured plausible nitrate stocks for the top 1 meter of soil: in the
923 range of 100-200 $\text{kg NO}_3^- \text{-N ha}^{-1}$ in croplands^{25,26} and less than 10 $\text{kg NO}_3^- \text{-N ha}^{-1}$ in forests.²⁷

924 Nitrogen removal in harvest could sometimes exceed N inputs, leading to implausibly
925 low NO_3^- concentrations. At locations where N surplus in croplands was less than 0.1 $\text{mol m}^{-2} \text{y}^{-1}$,
926 we assumed that imbalances in the N budget were being met by an unknown source (e.g.,
927 decomposition of soil organic matter or higher than 20% manure recoverability). In these cases,
928 we assigned a minimum value of 0.1 $\text{mol m}^{-2} \text{y}^{-1}$ for the net nitrogen balance before applying
929 losses from NO_3^- leaching and volatilization. This minimum value maintained cropland NO_3^-
930 levels within reported ranges.^{25,26}

931 Cropland C budgets were also adjusted to account for import and export of C in
932 agriculture. We adjusted NPP in croplands to account for removal of crop biomass, which
933 accounts for 43% of cropland NPP.²⁸ We also accounted for C introduced with manure. We
934 assumed a molar C:N ratio of 10 for manure, and used this number to scale manure C based on
935 county-level estimates for manure N.

936 We also considered cropland nutrient budgets for some additional nutrients. For
937 simplicity, we assumed that S and K inputs in fertilizer equaled outputs; hence Cs and Ck were
938 set equal to zero. For Ca and Mg, we accounted for inputs in manure and ag-lime and outputs in
939 crop harvest. Manure inputs were constrained by assigning Ca:N and Mg:N values for manure

940 and scaling Ca and Mg inputs to the manure N application rate. Ca:N and Mg:N for manure were
941 averaged across dairy solids, swine solids, and poultry manure types.²⁹ Similarly, average Ca:N
942 and Mg:N values were assigned for crop biomass using published values for corn and soy,³⁰
943 allowing us to approximate Ca and Mg removal in harvest.

944 We modeled liming rates endogenously as a function of pH. We first aligned county level
945 liming data from 1987[³¹] (the most recent available date) with maps of soil pH derived from
946 NATSGO.³² We assigned a pH value to croplands in each county by extracting NATSGO pH
947 values in a 10 km grid across the USA and masking out non-cropland areas using the GFSAD
948 cropland mask.³³ We then calculated the median cropland pH value in each county. This revealed
949 that liming rates vary widely below pH 7, but are low above pH 7. We modeled the maximum
950 rate of lime addition as a function of pH using a sigmoid function:

951 $\text{Lime}_{\text{max}} = p_1 * (1 - \exp(-10^{-p_{\text{Hlab}}/p_2})^{p_3})$ (Equation 20)

952 Where Lime_{max} was the maximum observed liming rate ($\text{t ha}^{-1} \text{ y}^{-1}$) p_1 , p_2 , and p_3 were
953 empirical constants and p_{Hlab} was the laboratory-measured soil pH assumed equal to the median
954 pH from NATSGO. We fit this function to the condition 90th percentiles of the data obtained in
955 0.5 pH-unit bins using the R function “nls”. The parameters received estimated values of $p_1 =$
956 0.424 , $p_2 = 1.42 * 10^{-7}$, and $p_3 = 1.13$.

957 Below the maximum liming rate, we assumed that farmers add enough lime to neutralize
958 acidity from fertilizer and replace Ca and Mg lost in crop biomass. Consequently, the main effect
959 of liming in the model was to maintain soil pH at the same level it would have attained under
960 unfarmed conditions. We made this assumption because it was a reasonable compromise between
961 two extreme alternatives: (1) assuming that farmers generally add lime aggressively to raise their

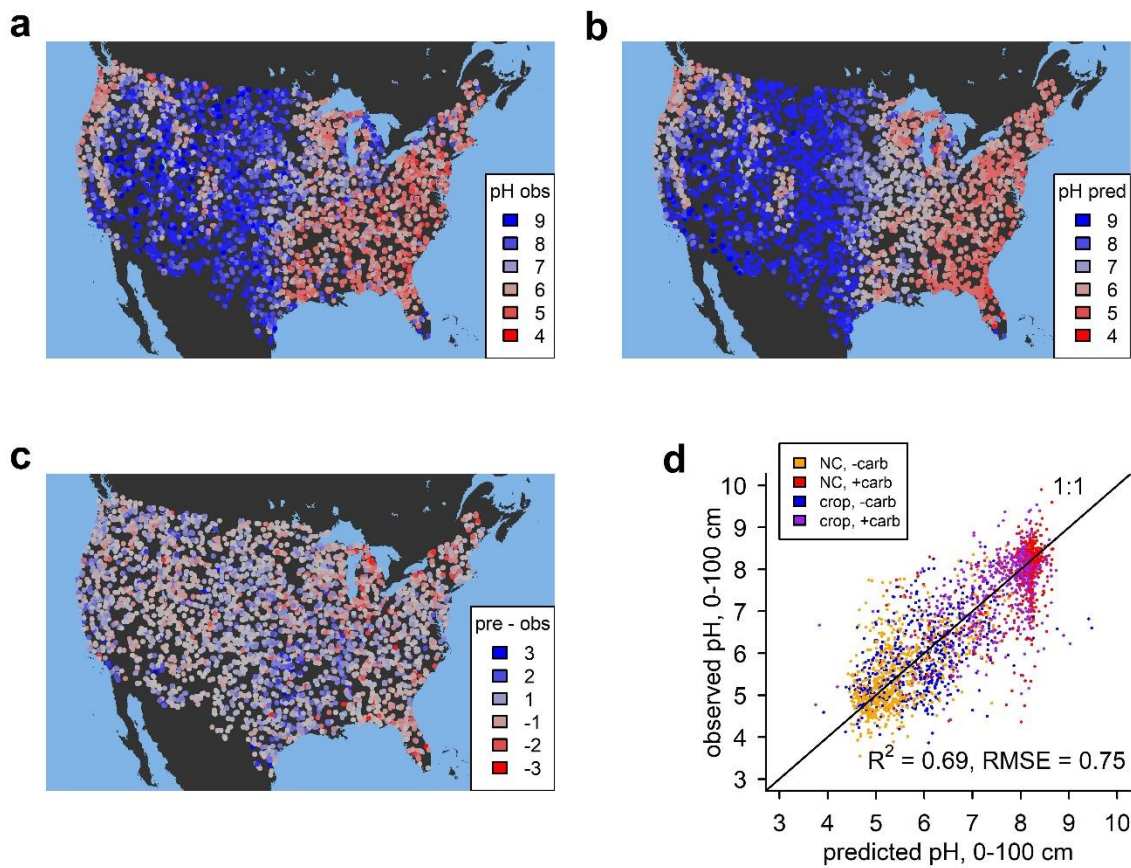
962 soil pH to agronomically optimal levels; or (2) farmers generally do not add enough lime to
963 maintain soil pH, and croplands are broadly acidified compared to unfarmed baseline conditions.
964 To estimate the liming rate, we first ran the model without agricultural influence, which yielded
965 the target pH value, pH_{target} . We then modeled lime addition as a function of pH_{lab} that increases
966 steeply towards $Lime_{max}$ at pH_{target} :

967
$$Lime_{tot} = Lime_{max} * (1 - \exp(-10^{-pH_{lab}}/10^{-pH_{target}})^{20}) \quad \text{Equation 21}$$

968 Applying this equation required approximating pH_{lab} because the model was designed to
969 calculate the in-situ field pH, while laboratory pH was estimated as a post-processing step at
970 some computational cost. To address this, we derived empirical linear relationships between the
971 in-situ pH and the laboratory pH prior to running cropland simulations, with a separate
972 relationship fitted for carbonate-buffered and carbonate free soils. These regressions explained
973 >90% of the variation in pH_{lab} and could be used to solve Equation 21 without explicitly
974 estimating this quantity at every model iteration, speeding up computations substantially.

975 After applying Equation 21, we partitioned lime added into calcitic and dolomitic
976 components. In general, crop Mg removal exceeded inputs, and so we satisfied Mg demand first.
977 Mg demand ($\text{mol m}^{-2} \text{ y}^{-1}$) was set equal to the cropland partial Mg budget (crop removal –
978 manure inputs) where removal exceeded inputs and set to zero elsewhere. Dolomitic lime
979 addition ($\text{mol m}^{-2} \text{ y}^{-1}$) was then set to equal to Mg demand. Where Mg demand could not be met
980 because the mass of dolomite added exceeded $Lime_{max}$, the cropland Mg budget was set equal to
981 zero and it was assumed the Mg came from other unknown sources. Calcitic lime addition was
982 calculated as the difference between the mass of dolomite added and $Lime_{tot}$. Ca and Mg added
983 in lime were obtained from dolomitic and calcitic lime based on the chemical formulae for
984 calcite and dolomite (Table S6).

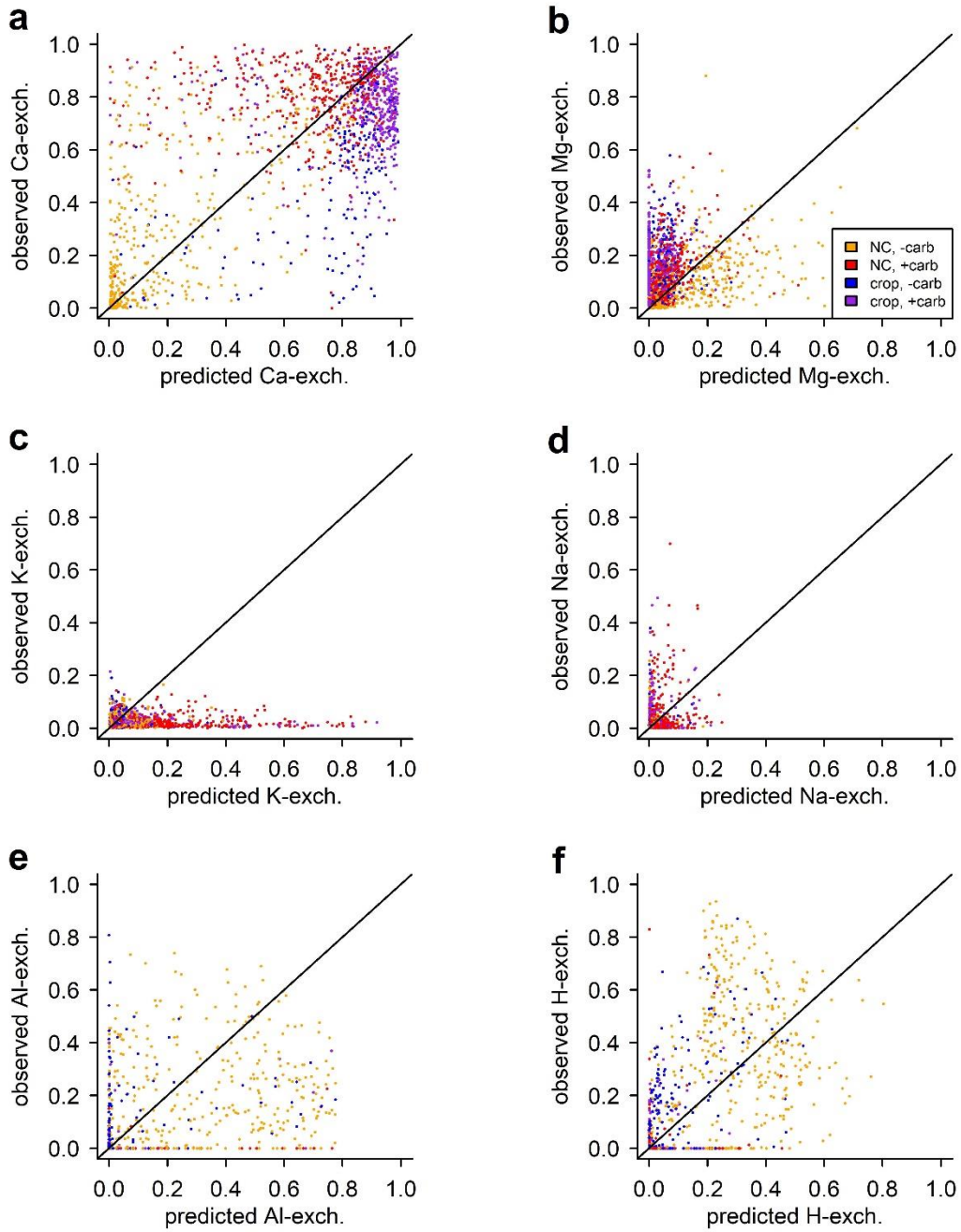
985



986

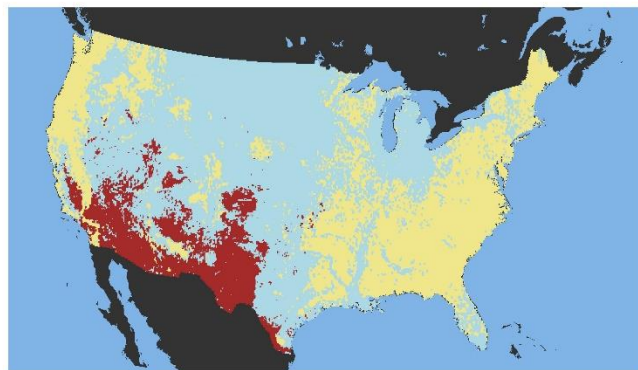
987 **Figure S1. Model performance matching soil pH.** (a) shows observed depth-weighted average
 988 soil pH of the top 100 cm at 4,247 unique locations used for model training and validation. (b)
 989 shows pH simulated by the calibrated model at the same locations, and (c) shows the model
 990 residuals (predicted – observed pH). (d) shows a plot of predicted versus observed pH, with
 991 colors representing different combinations of land use and soil carbonate status (NC, -carb =
 992 non-cropland, carbonate free; NC, +carb = non-cropland, carbonates present; crop, -carb =
 993 cropland, carbonate free; crop, +carb = cropland, carbonates present). RMSE is the root mean
 994 squared error.

995



996

997 **Figure S2. Model performance for exchangeable ions.** (a) – (f) show predicted versus
 998 observed exchange fractions for Ca, Mg, K, Na, Al, and H⁺. Observed values represent depth-
 999 weighted averages to 100 cm taken from the NCSS database³⁵ (n = 2,563 unique profiles).
 1000 Values are normalized by total cation exchange capacity (moles cation charge / CEC). Colors
 1001 represent different combinations of land use and soil carbonate status (NC, -carb = non-cropland,
 1002 carbonate free; NC, +carb = non-cropland, carbonates present; crop, -carb = cropland, carbonate
 1003 free; crop, +carb = cropland, carbonates present). Diagonal lines show the 1:1 relationship.



Carbonate Ca source/sink status

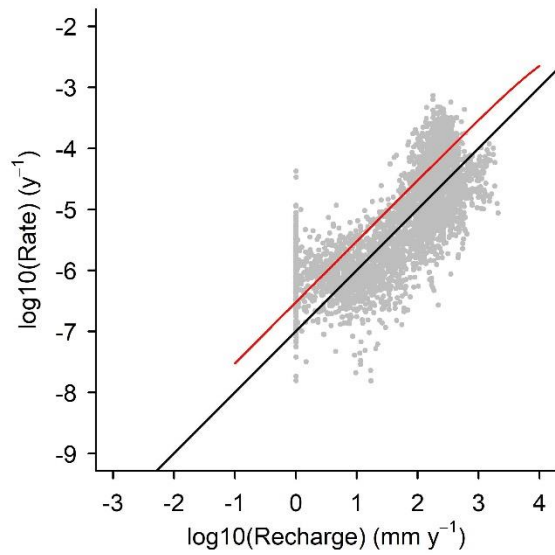
■ source ■ absent ■ sink

1004

1005 **Figure S3. Modeled carbonate source / sink status.** Data show model simulations under
1006 preindustrial late Holocene conditions. Areas mapped in yellow are carbonate free, areas mapped
1007 in blue are releasing Ca via carbonate weathering, and areas mapped in red are a sink for Ca via
1008 carbonate formation.

1009

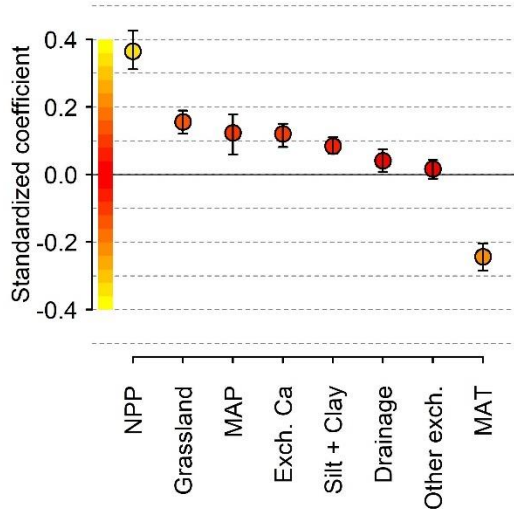
1010



1011

1012 **Figure S4. Modeled plagioclase feldspar weathering rate versus recharge.** Gray points show
1013 modeled feldspar weathering rates normalized by the feldspar stock versus the recharge
1014 parameter. The red line shows the non-linear fit to a compilation of field and lab weathering rates
1015 from Maher 2010,[³] and the black line shows a fit to the same compilation from Yu and Hunt
1016 2018[⁴].

1017



1018

1019 **Figure S5. Controls on A-horizon soil organic carbon stocks in the USA, with corrected**
 1020 **CEC.** Standardized regression coefficients were derived from a multivariate linear regression
 1021 model, where A-horizon organic carbon stocks were predicted as a function of the eight variables
 1022 listed on the horizontal axis. In this case, cation exchange capacity (CEC) was corrected for the
 1023 contribution from soil organic matter prior to calculating exchangeable ion pools. In both panels,
 1024 whiskers show 95% confidence intervals derived from a spatial blocked bootstrapping procedure
 1025 (see Methods). The absolute value of each regression coefficient is an index of how strongly
 1026 related each variable is to the response variable, and is shown with a relative color scale: yellow
 1027 = maximum, red = zero. Abbreviations: NPP = net primary productivity, MAT = mean annual
 1028 temperature, MAP = mean annual precipitation, Exch. Ca = total exchangeable Ca, Other exch. =
 1029 sum of non-Ca exchangeable ions.

1030

1031

	R²	RMSE
Ca ²⁺	0.39	0.27
Mg ²⁺	0.03	0.15
Na ⁺	0.06	0.06
K ⁺	0	0.16
Al ³⁺	0.27	0.17
H ⁺	0.45	0.16
All	0.64	0.17

1032

1033 **Table S1. Validation statistics for exchangeable ions.** R² values are derived by regressing
 1034 observations on predictions; root mean squared error (RMSE) was calculated as the square root
 1035 of the mean of the squared residuals (geochemical model predictions – observations). Statistics
 1036 for all cations were obtained by treating all observed and predicted cation fractions as
 1037 independent values and pooling them. Observed values represent depth-weighted averages to 100
 1038 cm taken from the NCSS database³⁵ (n = 2,563 unique profiles; 3,423 total including repeats
 1039 from spatially weighted resampling). Values are normalized by total cation exchange capacity
 1040 (moles cation charge / CEC).

1041

1042

	value	CI
intercept	-2.342	[-2.644, -2.082]
grassland	1.45	[1.205, 1.695]
base sat.	2.887	[2.433, 3.544]
silt + clay	-1.333	[-1.706, -1.004]
NPP	0.202	[-0.048, 0.451]
Drainage	0.724	[0.470, 1.039]
MAT	0.644	[0.253, 0.994]
MAP	-0.638	[-1.102, -0.162]

1043

1044 **Table S2. Results of logistic regression analysis for Mollisol extent.** Statistics are derived from
 1045 a multivariate logistic regression, where the presence or absence of Mollisols was modeled as a
 1046 function of potential grassland and savanna vegetation (grassland), base saturation (base sat.),
 1047 soil silt + clay content, net primary productivity (NPP), USDA drainage class (drainage), Mean
 1048 annual temperature (MAT), and mean annual precipitation (MAP). Continuous predictors were
 1049 scaled by their standard deviations prior to fitting, whereas the binary predictor (grassland) was
 1050 scaled by two times its standard deviation. Model null deviance = 136,055; Residual deviance =
 1051 97075. At a probability threshold of 0.4 the accuracy rate was 0.79; sensitivity was 0.61; and
 1052 specificity was 0.86. Confidence intervals were derived from a spatially blocked bootstrapping
 1053 procedure (see Methods).

1054

	value	CI
intercept	-0.051	[-0.067, -0.036]
NPP	0.143	[0.106, 0.172]
MAP	0.152	[0.120, 0.185]
exch. Ca	0.013	[-0.014, 0.039]
grassland	-0.233	[-0.270, -0.188]
silt + clay	0.029	[-0.005, 0.062]
Drainage	0.079	[0.057, 0.103]
other exch.	0.362	[0.304, 0.421]
MAT	0.13	[0.069, 0.179]

1055

1056 **Table S3. Results of multiple regression analysis for A-horizon SOC.** Statistics are derived
 1057 from a multivariate logistic regression, where log-transformed A-horizon organic carbon stocks
 1058 were modeled as a function of potential grassland and savanna vegetation (grassland),
 1059 exchangeable Ca (Ca exch.), non-Ca exchangeable ions (other exch.), soil silt + clay content, net
 1060 primary productivity (NPP), USDA drainage class (drainage), Mean annual temperature (MAT),
 1061 and mean annual precipitation (MAP). Continuous predictors were scaled by their standard
 1062 deviations prior to fitting, whereas the binary predictor (grassland) was scaled by two times its
 1063 standard deviation. Model $R^2 = 0.30$ and residual standard error was 0.4189. Confidence
 1064 intervals were derived from a spatially blocked bootstrapping procedure (see Methods).

Ion or algebraic constraint	Equation
Ca^{2+}	$d\text{Ca}/dt = D_{\text{Ca}} + A_{\text{Ca}} + C_{\text{Ca}} + R_{\text{Cc,Ca}} + R_{\text{Do,Ca}} + R_{\text{Pl,Ca}} + R_{\text{Hb,Ca}} + R_{\text{Py,Ca}} - L_{\text{Ca}}$
Mg^{2+}	$d\text{Mg}/dt = D_{\text{Mg}} + A_{\text{Mg}} + C_{\text{Mg}} + R_{\text{Do,Mg}} + R_{\text{Hb,Mg}} + R_{\text{Py,Mg}} + R_{\text{Cl,Mg}} - L_{\text{Mg}}$
Na^+	$d\text{Na}/dt = D_{\text{Na}} + R_{\text{Pl,Na}} - L_{\text{Na}}$
K^+	$d\text{K}/dt = D_{\text{K}} + C_{\text{K}} + M_{\text{K}} + R_{\text{Ks,K}} + R_{\text{Il,K}} - U_{\text{K}} - L_{\text{K}}$
NO_3^-	$d\text{N}/dt = D_{\text{N}} + C_{\text{N}} + F_{\text{N}} - V_{\text{N}} - L_{\text{N}}$
SO_4^{2-}	$d\text{S}/dt = D_{\text{S}} + C_{\text{S}} - L_{\text{S}}$
Cl^-	$d\text{Cl}/dt = D_{\text{Cl}} - L_{\text{Cl}}$
Charge Balance	$0 = (2[\text{Ca}^{2+}] + 2[\text{Mg}^{2+}] + [\text{K}^+] + [\text{Na}^+] + 3[\text{Al}^{3+}] + 2[\text{Al}(\text{OH})^{2+}] + [\text{Al}(\text{OH})_2^{+}] + 2[\text{AlH}^{2+}] + [\text{AlH}_2\text{Org}^+] + [\text{H}^+] - ([\text{OH}^-] + [\text{HCO}_3^-] + 2[\text{CO}_3^{2-}] + [\text{H}_2\text{Org}^-] + 2[\text{H}^{+}] + 2[\text{Org}^{3-}] + 3[\text{Org}^{3-}] + [\text{Al}(\text{OH})_4^-] + 2[\text{SO}_4^{2-}] + [\text{NO}_3^-] + [\text{Cl}^-])$
Exchange	$1 = f\text{Ca} + f\text{Mg} + f\text{Na} + f\text{K} + f\text{Al} + f\text{H}$

1065 **Table S4 Governing equations.** Capital letters indicate rates: D = deposition (wet + dry); A =
 1066 agricultural liming, C = cropland nutrient budget (inputs – uptake); R = weathering; L =
 1067 leaching; F = fixation; V = volatilization. Weathering rates ($\text{mol mineral y}^{-1}$) were multiplied by
 1068 the molar concentration of each element the mineral to yield the flux of each element from the
 1069 mineral; this is indicated in the subscripts, with the mineral listed first and then the
 1070 corresponding element. Minerals: Cc = calcite; Do = dolomite; Pl = plagioclase; Hb =
 1071 hornblende; Py = pyroxene; Cl = chlorite; Ks = K-feldspar; Il = illite.

1072

Parameter	Description	Value	Units	Source
E _{a,sil}	Silicate weathering activation energy	74	kJ mol ⁻¹ K ⁻¹	²
H _r	Reference [H ⁺] value	10 ⁻⁵	mol l ⁻¹	This study
n _H	Silicate weathering reaction order for H ⁺	0.6667	-	This study
RRP ₁	Relative reaction rate, plagioclase	1	-	^{1 *}
RRK _s	Relative reaction rate, K-feldspar	0.63	-	^{1 *}
RRH _b	Relative reaction rate, hornblende	0.25	-	^{1 *}
RRP _y	Relative reaction rate, pyroxene	1	-	This study
log(A _{acid,Cc})	Acid mechanism preexponential factor, calcite	-0.3	mol m ⁻² s ⁻¹	⁶
log(A _{neut,Cc})	Neutral mechanism preexponential factor, calcite	-5.81	mol m ⁻² s ⁻¹	⁶
log(A _{CO2,Cc})	CO ₂ mechanism preexponential factor, calcite	-3.48	mol m ⁻² s ⁻¹	⁶
log(A _{acid,Do})	Acid mechanism preexponential factor, dolomite	-3.19	mol m ⁻² s ⁻¹	⁶
log(A _{neut,Do})	Neutral mechanism preexponential factor, dolomite	-7.53	mol m ⁻² s ⁻¹	⁶
log(A _{CO2,Do})	CO ₂ mechanism preexponential factor, dolomite	-5.11	mol m ⁻² s ⁻¹	⁶
E _{a,acid,cc}	Acid mechanism activation energy, calcite	14.4	kJ mol ⁻¹ K ⁻¹	⁶
E _{a,neut,cc}	Neutral mechanism activation energy, calcite	23.5	kJ mol ⁻¹ K ⁻¹	⁶
E _{a,CO2,cc}	CO ₂ mechanism activation energy, calcite	35.4	kJ mol ⁻¹ K ⁻¹	⁶
E _{a,acid,do}	Acid mechanism activation energy, dolomite	36.1	kJ mol ⁻¹ K ⁻¹	⁶
E _{a,neut,do}	Neutral mechanism activation energy, dolomite	52.2	kJ mol ⁻¹ K ⁻¹	⁶
E _{a,CO2,do}	CO ₂ mechanism activation energy, dolomite	34.8	kJ mol ⁻¹ K ⁻¹	⁶
nH _{Cc}	Reaction order for H ⁺ , calcite	1	-	⁶
nCO _{2,Cc}	Reaction order for CO ₂ , calcite	1	-	⁶
nH _{Do}	Reaction order for H ⁺ , dolomite	0.5	-	⁶
nCO _{2,Do}	Reaction order for CO ₂ , dolomite	0.5	-	⁶

1073

Table S5 Weathering rate parameters

1074

1075

Mineral	Abbr.	Type	Formula	Density
Plagioclase	Pl	tectosilicate	$\text{Na}_{(1-f_{\text{An}})}\text{Ca}_{f_{\text{An}}}\text{Al}_{(1+f_{\text{An}})}\text{Si}_{(3-f_{\text{An}})}\text{O}_8$	$2.75f_{\text{An}} + 2.625(1-f_{\text{An}})$
K-feldspar	Ks	tectosilicate	KAlSi_3O_8	2.59
Pyroxene	Py	inosilicate	$\text{MgCa}(\text{SiO}_3)_2$	3.3
Hornblende	Hb	inosilicate	$\text{Ca}_2(\text{Mg}_2\text{Fe}_2\text{Al})\text{Si}_7\text{AlO}_{22}(\text{OH})_2$	3.1735
Chlorite	Cl	phyllosilicate	$\text{Mg}_5\text{Al}_2\text{Si}_3\text{O}_{18}\text{H}_8$	2.915
Illite	Il	phyllosilicate	$\text{K}(\text{Al}_2)(\text{Si}_3\text{Al})\text{O}_{10}(\text{OH})_2$	2.795
Calcite	Cc	carbonate	CaCO_3	2.7102
Dolomite	Do	carbonate	$\text{CaMg}(\text{CO}_3)_2$	2.85

1076 **Table S6 Mineral properties.** f_{An} = anorthite molar fraction. Densities are midpoints of reported
 1077 ranges from Mindat.org.

1078

Reaction	$\Delta S \text{ (kJ K}^{-1} \text{ mol}^{-1}\text{)}$	$\Delta H \text{ (kJ mol}^{-1}\text{)}$	logK	source
$\text{CO}_2 \text{ (g)} \leftrightarrow \text{CO}_2 \text{ (aq)}$	-0.09616924	-20.28821600		8,9
$\text{CO}_2 \text{ (aq)} + \text{H}_2\text{O} \leftrightarrow \text{HCO}_3^- + \text{H}^+$	-0.08904506	9.70167230		8,9
$\text{HCO}_3^- \leftrightarrow \text{CO}_3^{2-} + \text{H}^+$	-0.14844832	14.69839200		8,9
$\text{H}_2\text{O} \leftrightarrow \text{OH}^- + \text{H}^+$	-0.08063522	55.81353630		8,9
$\text{Al(OH)}_3 \text{ (s)} \leftrightarrow \text{Al(OH)}_3 \text{ (aq)}$	-0.00908996	50.45803923		8,9
$\text{Al(OH)}_3 \text{ (aq)} + 3\text{H}^+ \leftrightarrow \text{Al}^{3+} + 3\text{H}_2\text{O}$	-0.18933085	-153.61153602		8,9
$\text{Al(OH)}_3 \text{ (aq)} + 2\text{H}^+ \leftrightarrow \text{Al(OH)}_2^+ + 2\text{H}_2\text{O}$	-0.10062704	-98.86893231		8,9
$\text{Al(OH)}_3 \text{ (aq)} + 1\text{H}^+ \leftrightarrow \text{Al(OH)}^{2+} + \text{H}_2\text{O}$	-0.01697332	-39.97106033		8,9
$\text{Al(OH)}_3 \text{ (aq)} + \text{H}_2\text{O} \leftrightarrow \text{Al(OH)}_4^- + \text{H}^+$	-0.02572859	25.43199965		8,9
$\text{CaCO}_3 \text{ (s)} \leftrightarrow \text{Ca}^{2+} + \text{CO}_3^{2-}$	-0.19820780	-11.49904000		8,9
$\text{CaMgC}_2\text{O}_6 \text{ (s)} \leftrightarrow \text{Ca}^{2+} + \text{Mg}^{2+} + 2\text{CO}_3^{2-}$	-0.44944386	-34.26448628		8,9
$\text{Mg}_5\text{Al}_2\text{Si}_3\text{O}_{18}\text{H}_8 \text{ (s)} + 10\text{H}^+ \leftrightarrow 2\text{Al(OH)}_3 \text{ (aq)} + 5\text{Mg}^{2+} + 3\text{H}_4\text{SiO}_2 \text{ (aq)}$	-0.08814278	-56.42611		8,9
$\text{KAl}_3\text{Si}_3\text{O}_{12}\text{H}_2 \text{ (s)} + \text{H}^+ + 9\text{H}_2\text{O} \leftrightarrow 3\text{Al(OH)}_3 \text{ (aq)} + \text{K}^+ + 3\text{H}_4\text{SiO}_2 \text{ (aq)}$	-0.0772809	199.2072		8,9
$\text{SiO}_2 \text{ (amorph)} + 2\text{H}_2\text{O} \leftrightarrow \text{H}_4\text{SiO}_4$	-0.01114692	10.56612		8,9
$\text{H}_3\text{Org} \leftrightarrow \text{H}_2\text{Org}^- + \text{H}^+$			-2.653	¹⁴
$\text{H}_2\text{Org}^- \leftrightarrow \text{H}\text{Org}^{2-} + \text{H}^+$			-6.233	¹⁴
$\text{H}\text{Org}^{2-} \leftrightarrow \text{Org}^{3-} + \text{H}^+$			-7.467	¹⁴
$\text{AlH}_2\text{Org}^{2+} \leftrightarrow \text{H}^+ + \text{AlH}\text{Org}^+$			-4.963	¹⁴
$\text{AlH}\text{Org}^+ \leftrightarrow \text{H}^+ + \text{AlOrg}$			-4.040	¹⁴
$\text{AlOrg} \leftrightarrow \text{Al}^{3+} + \text{Org}^{3-}$			-10.020	¹⁴
$3\text{Ca-X} + 2\text{Al}^{3+} \leftrightarrow 2\text{Al-X} + 3\text{Ca}^{2+}$			2.026 (s); 1.195 (lo); 0.106 (cl)	¹⁶
$3\text{Mg-X} + 2\text{Al}^{3+} \leftrightarrow 2\text{Al-X} + 3\text{Mg}^{2+}$			2.811 (s); 1.244 (lo); 0.599 (cl)	¹⁶
$3\text{Na-X} + \text{Al}^{3+} \leftrightarrow \text{Al-X} + 3\text{Na}^+$			1.811 (s); 0.646 (lo); 1.045 (cl)	¹⁶
$3\text{K-X} + \text{Al}^{3+} \leftrightarrow \text{Al-X} + 3\text{K}^+$			-0.917 (s); -2.413 (lo); -3.561 (cl)	¹⁶
$3\text{H-X} + \text{Al}^{3+} \leftrightarrow \text{Al-X} + 3\text{H}^+$			-6.924 (s); -7.532 (lo); -9.923 (cl)	¹⁶

1079 **Table S7 Equilibrium reactions and thermodynamic parameters.** For exchange reactions
1080 logK values are for sand, loess, and clay respectively based on reference [9].

1082 **References**

1083 1. White, A. F. & Buss, H. L. Natural Weathering Rates of Silicate Minerals. in *Treatise on*
1084 *Geochemistry* 115–155 (Elsevier, 2014). doi:10.1016/B978-0-08-095975-7.00504-0.

1085 2. West, A., Galy, A. & Bickle, M. Tectonic and climatic controls on silicate weathering. *Earth*
1086 and *Planetary Science Letters* **235**, 211–228 (2005).

1087 3. Maher, K. The dependence of chemical weathering rates on fluid residence time. *Earth and*
1088 *Planetary Science Letters* **294**, 101–110 (2010).

1089 4. Yu, F. & Hunt, A. G. Predicting soil formation on the basis of transport-limited chemical
1090 weathering. *Geomorphology* **301**, 21–27 (2018).

1091 5. Slessarev, E. W. *et al.* Water balance creates a threshold in soil pH at the global scale. *Nature*
1092 **540**, 567–569 (2016).

1093 6. Palandri & Kharaka, Y. A compilation of rate parameters of water-mineral interaction
1094 kinetics for application to geochemical modeling. (2004).

1095 7. Swoboda-Colberg, N. G. & Drever, J. I. Mineral dissolution rates in plot-scale field and
1096 laboratory experiments. *Chemical Geology* **105**, 51–69 (1993).

1097 8. Johnson, J. W., Oelkers, E. H. & Helgeson, H. C. SUPCRT92: A software package for
1098 calculating the standard molal thermodynamic properties of minerals, gases, aqueous
1099 species, and reactions from 1 to 5000 bar and 0 to 1000°C. *Computers & Geosciences* **18**,
1100 899–947 (1992).

1101 9. Dick, J. M. CHNOSZ: Thermodynamic Calculations and Diagrams for Geochemistry. *Front.*
1102 *Earth Sci.* **7**, 180 (2019).

1103 10. Gaillardet, J., Calmels, D., Romero-Mujalli, G., Zakharova, E. & Hartmann, J. Global
1104 climate control on carbonate weathering intensity. *Chemical Geology* **527**, 118762 (2019).

1105 11. Lan, X. & Keeling, R. Trends in atmospheric carbon dioxide.

1106 12. Etheridge, D. M. *et al.* Natural and anthropogenic changes in atmospheric CO₂ over the last
1107 1000 years from air in Antarctic ice and firn. *J. Geophys. Res.* **101**, 4115–4128 (1996).

1108 13. Raich, J. W. & Schlesinger, W. H. The global carbon dioxide flux in soil respiration and its
1109 relationship to vegetation and climate. *Tellus B* **44**, 81–99 (1992).

1110 14. Fakhraei, H. & Driscoll, C. T. Proton and Aluminum Binding Properties of Organic Acids in
1111 Surface Waters of the Northeastern U.S. *Environ. Sci. Technol.* **49**, 2939–2947 (2015).

1112 15. Camino-Serrano, M. *et al.* ORCHIDEE-SOM: modeling soil organic carbon (SOC) and
1113 dissolved organic carbon (DOC) dynamics along vertical soil profiles in Europe. *Geosci.*
1114 *Model Dev.* **11**, 937–957 (2018).

1115 16. Vries, W. & Posch, M. Derivation of cation exchange constants for sand, loess, clay and peat
1116 soils on the basis of field measurements in the Netherlands. (2003).

1117 17. Kanzaki, Y., Chiaravalloti, I., Zhang, S., Planavsky, N. J. & Reinhard, C. T. In silico
1118 calculation of soil pH by SCEPTER v1.0. *Geosci. Model Dev.* **17**, 4515–4532 (2024).

1119 18. Posch, M. & Reinds, G. J. A very simple dynamic soil acidification model for scenario
1120 analyses and target load calculations. *Environmental Modelling & Software* **24**, 329–340
1121 (2009).

1122 19. Wieder, W. R., Cleveland, C. C., Lawrence, D. M. & Bonan, G. B. Effects of model
1123 structural uncertainty on carbon cycle projections: biological nitrogen fixation as a case
1124 study. *Environ. Res. Lett.* **10**, 044016 (2015).

1125 20. Wymore, A. S. *et al.* Gradients of Anthropogenic Nutrient Enrichment Alter N Composition
1126 and DOM Stoichiometry in Freshwater Ecosystems. *Global Biogeochemical Cycles* **35**,
1127 e2021GB006953 (2021).

1128 21. Swaney, D. P., Howarth, R. W. & Hong, B. Nitrogen use efficiency and crop production:
1129 Patterns of regional variation in the United States, 1987–2012. *Science of The Total*
1130 *Environment* **635**, (2018).

1131 22. Smil, V. Nitrogen in crop production: An account of global flows. *Global Biogeochemical*
1132 *Cycles* **13**, 647–662 (1999).

1133 23. Kellogg, R. L., Lander, C. H., Moffitt, D. C. & Gollehon, N. Manure nutrients relative to the
1134 capacity of cropland and pastureland to assimilate nutrients: Spatial and temporal trends for
1135 the United States. (2000).

1136 24. Velthof, G. L. *et al.* Integrated Assessment of Nitrogen Losses from Agriculture in EU-27
1137 using MITERRA-EUROPE. *J of Env Quality* **38**, 402–417 (2009).

1138 25. Roth, G. W. & Fox, R. H. Soil Nitrate Accumulations following Nitrogen-Fertilized Corn in
1139 Pennsylvania. *J of Env Quality* **19**, 243–248 (1990).

1140 26. Ziadi, N., Bélanger, G. & Claessens, A. Relationship between soil nitrate accumulation and
1141 in-season corn N nutrition indicators. *Can. J. Plant Sci.* **92**, 331–339 (2012).

1142 27. Xu-Ri & Prentice, I. C. Terrestrial nitrogen cycle simulation with a dynamic global
1143 vegetation model. *Global Change Biology* **14**, 1745–1764 (2008).

1144 28. West, T. O., Bandaru, V., Brandt, C. C., Schuh, A. E. & Ogle, S. M. Regional uptake and
1145 release of crop carbon in the United States. *Biogeosciences* **8**, 2037–2046 (2011).

1146 29. Animal Manure Production and Utilization in the US. in *Applied Manure and Nutrient*
1147 *Chemistry for Sustainable Agriculture and Environment* 1–21 (Springer Netherlands,
1148 Dordrecht, 2014). doi:10.1007/978-94-017-8807-6_1.

1149 30. Masters, M. D. *et al.* Soil nutrient removal by four potential bioenergy crops: *Zea mays*,
1150 *Panicum virgatum*, *Miscanthus*×*giganteus*, and prairie. *Agriculture, Ecosystems &*
1151 *Environment* **216**, 51–60 (2016).

1152 31. Haines, M., Fishback, P. & Rhode, P. United States Agriculture Data, 1840 - 2012: Version 4.

1153 ICPSR - Interuniversity Consortium for Political and Social Research
1154 <https://doi.org/10.3886/ICPSR35206.V4> (2014).

1155 32. Soil Survey Staff. Gridded National Soil Survey Geographic (gNATSGO) Database for the
1156 Conterminous United States.

1157 33. Teluguntla, P. *et al.* NASA Making Earth System Data Records for Use in Research
1158 Environments (MEaSURES) Global Food Security Support Analysis Data (GFSAD) Crop
1159 Mask 2010 Global 1 km V001. NASA Land Processes Distributed Active Archive Center
1160 <https://doi.org/10.5067/MEASURES/GFSAD/GFSAD1KCM.001> (2016).

1161 34. West, T. O. & McBride, A. C. The contribution of agricultural lime to carbon dioxide
1162 emissions in the United States: dissolution, transport, and net emissions. *Agriculture,*
1163 *Ecosystems & Environment* **108**, 145–154 (2005).

1164 35. National Cooperative Soil Survey. National Cooperative Soil Survey Soil Characterization
1165 Database. (2018).

1166

1167